Astronomy and Astrophysics Supplement Series, Ulysses Instruments Special Issue, Vol. 92, No. 2, pp. 291-316, Jan. 1992. Copyright 1992 European Southern Observatory. Reprinted by permission.

Astron. Astrophys. Suppl. Ser. 92, 291-316 (1992)

ASTRONOMY & ASTROPHYSICS
SUPPLEMENT SERIES

JANUARY 1992, PAGE 291

*Astron. Astrophys. Suppl. Ser.* **92**, 291-316 (1992)

# The unified radio and plasma wave investigation

R.G. Stone[1], J.L. Bougeret[2], J. Caldwell[1], P. Canu[3], Y. de Conchy[2], N. Cornilleau-Wehrlin[3], M.D. Desch[1], J. Fainberg[1], K. Goetz[4], M.L. Goldstein[1], C.C. Harvey[2], S. Hoang[2], R. Howard[4], M.L. Kaiser[1], P.J. Kellogg[4], B. Klein[1], R. Knoll[2], A. Lecacheux[2], D. Lengyel-Frey[1], R.J. MacDowall[1], R. Manning[2], C.A. Meetre[1], A. Meyer[3], N. Monge[2], S. Monson[4], G. Nicol [2], M.J. Reiner[1], J.L. Steinberg[2], E. Torres[1], C. de Villedary[3], F. Wouters[2] and P. Zarka[2]

[1] NASA Goddard Space Flight Center (GSFC), Greenbelt, Maryland, 20771, U.S.A.
[2] Observatoire de Paris-Meudon, 92190 Meudon, France
[3] Centre de Recherches en Physique de l'Environment Terrestre et Planetaire (CRPE) CRPE/CNET/CNRS, 92131 Issy-les-Moulineaux, France
[4] University of Minnesota, School of Physics and Astronomy, Minneapolis, Minnesota, 55455, U.S.A.

*Received April 17; accepted July 19, 1991*

**Abstract.** — The scientific objectives of the Ulysses Unifiewd Radio and Plasma wave (URAP) experiment are twofold: 1) the determination of the direction, angular size, and polarization of radio sources for remote sensing of the heliosphere and the Jovian magnetosphere and 2) the detailed study of local wave phenomena, which determine the transport coefficients of the ambient plasma. The tracking of solar radio bursts, for example, can provide three dimensional "snapshots" of the large scale magnetic field configuration along which the solar exciter particles propagate. URAP observations of Jovian radio emissions should greatly improve the determination of source locations and consequently our understanding of the generation mechanism(s) of planetary radio emissions. The study of observed wave-particle interactions will improve our understanding of the processes that occur in the solar wind and at Jupiter and of radio wave generation. A brief discussion of the scientific goals of the experiment is followed by a comprehensive description of the instrument. The URAP sensors consist of a 72.5 m electric field antenna in the spin plane, a 7.5-m electric field monopole along the spin axis and a pair of orthogonal search coil magnetic antennas. The various receivers, designed to encompass specific needs of the investigation, cover the frequency range from DC to 1 MHz. A relaxation sounder provides very accurate electron density measurements. Radio and plasma wave observations are shown to demonstrate the capabilities and limitations of the URAP instruments: radio observations include solar bursts, auroral kilometric radiation, and Jovian bursts; plasma waves include Langmuir waves, ion acoustic-like noise, and whistlers.

**Key words:** Space vehicles — Radio emissions from the Sun — Solar wind — Interplanetary medium — Magnetosphere of Jupiter — Plasmas.

## 1. Scientific Objectives.

The solar wind is a microcosm of interstellar, galactic and extragalactic space. Indeed, except for the planets, most of space is filled with ionized matter called plasma. For this reason a major goal is to study the solar wind, our only accessible astrophysical plasma, under as wide a range of physical conditions as possible. In the context of this paper, the term *plasma waves* characterizes all waves that are generated in a plasma or that have their wave characteristics significantly modified by the presence of a plasma. These waves may be predominantly electromagnetic, having both electric and magnetic fields produced by current fluctuations, or electrostatic, having only an electric field produced by charge fluctuations. Naturally-occuring waves are generated by the conversion of plasma and energetic particle kinetic energy into wave energy through a variety of wave-particle processes. In turn, these waves may interact with the particles and modify the distribution function characteristic of the particle populations within the plasma. Some electromagnetic waves manage to propagate far enough from the source region for their frequency to be well removed from the characteristic frequencies of the ambient medium. The observation of these radio waves provides information on the remote source region.

Radio and plasma waves are present throughout the heliosphere. They are the signature of phenomena of fun-

---

*Send offprint requests to*: R.G. Stone.

damental importance to our understanding of the physics of the plasma that fills the heliosphere. The Ulysses Unified Radio and Plasma Wave (URAP) experiment comprises a complete set of wave-measuring instruments, including a radio receiver to study radio emission generated in distant regions and a battery of plasma wave instruments designed to analyze *in-situ* plasma waves.

Figure 1 shows the wide variety of phenomena which can be observed with just one of the URAP instruments. The figure is a dynamic spectrum observed on January 4, 1991 by the Radio Astronomy Receiver portion of the URAP. The abscissa is time and the ordinate scale shows observing frequency. A color intensity scale is included in the figure. Examples of type III solar radio bursts, terrestrial auroral kilometric radiation, Jupiter emissions and the thermal plasma line can be seen in the figure. In Section 3, each of these phenomena will be discussed in greater detail along with observations from the other URAP instruments.

The study of the heliosphere in three dimensions requires a description of the large-scale distribution of the solar-wind plasma and the embedded magnetic field. From Parker's work (Parker, 1963) and subsequent space observations, it is known that the magnetic lines of force are wound in spirals because of the coupling between the radial expansion of the solar wind and solar rotation. However, the strong inhomogeneity of the solar surface disturbs the flow structure in a way which is not fully understood: the structure of the solar wind is much more complicated than predicted from Parker's theory. Ground based observations and space observations near the ecliptic show that solar wind characteristics vary rapidly with heliocentric latitude, but these observations are generally limited to an excursion in latitude of 7°, except for radio scintillation observations, which, in turn, are restricted to relatively small heliocentric distances (Coles & Rickett, 1986; Bhonsle *et al.*, 1986). Pioneer-11 did not detect any trace of sector structure at a heliographic latitude of only 16°.

The large-scale structure of the interplanetary magnetic field is important for understanding the propagation of high energy particles in the heliosphere. There is evidence for large deviations from a radial geometry in the vicinity of active centers at low coronal latitudes, which have implications for the propagation of Sun-ejected particles. We still do not understand the origin of the modulation of cosmic rays by solar activity. Is it through small scale, activity-dependent fluctuations of the magnetic field or through large-scale variations in the topology? Several studies have shown that drift motions of ions and electrons almost certainly play a role just prior to the onset of a new modulation cycle and at other periods during the 22-year period (Jokipii & Kota 1989). In the outer heliosphere, the decreases in the cosmic ray intensity appear to be associated with the passage of merged interaction regions (Burlaga *et al.* 1991).

Several approaches are used to map the large scale heliospheric magnetic field (Hoeksema, 1986; Fry & Akasofu, 1986) using models of the fluid flow together with maps of solar surface fields and interplanetary magnetometer data. These methods are generally limited to the plane of the ecliptic or, at most, the latitudes reached by Pioneer and Voyager in the outer heliosphere. Recently, Wang *et al.* (1990) have proposed a method for studying the out-of-ecliptic solar wind, using a correlation between the solar wind speed near the Earth and the magnetic field in the solar corona. There is another method, however, which can in principle produce three-dimensional traces of the interplanetary fields. This technique uses the emission from type III solar radio bursts. Solar type III bursts are radio waves emitted near the fundamental and/or second harmonic of the local electron plasma frequency by beams of electrons having energies in the range 2–30 keV (Lin, 1985; Dulk, 1985). Since the electron beams travel along magnetic lines of force (Fainberg *et al.* 1972), tracking these solar events at a number of radio frequencies allows one to remotely determine the local plasma frequency (and hence the local electron density) at each location, and to map the magnetic lines of force along which the electrons travel (Fitzenreiter *et al.* 1977). From the curvature of the field one can also estimate the solar wind velocity (Bougeret *et al.* 1983).

Interplanetary shocks can be studied from the type II radio waves which they emit (Lengyel-Frey & Stone, 1989). Solar type II bursts, like type III bursts, are radio emissions close to the fundamental and/or second harmonic of the local electron plasma frequency, but type II bursts are associated with electrons accelerated in the vicinity of travelling shock waves in the solar corona and interplanetary medium. The frequency of type II emission at a given time provides an indication of the distance of the shock from the Sun. Shocks may also be located by their effects on type III radio bursts (MacDowall 1989).

To relate the overall flow pattern of the solar wind to conditions in the low corona, it is necessary to describe the local properties of the flowing plasma. The solar-wind plasma is certainly not collision dominated since at 1 AU the collision mean free path is of order 1 AU. Nonetheless, many properties of the medium are describable by fluid equations. In large measure the role of Coulomb collisions is played by wave-particle interactions which reduce the effective mean-free-path to $\approx 10^4$ km, the typical size of many observed structures in the solar wind. The study of the origin and nature of the fluid properties of the solar wind is still an active area of research.

An example of wave-particle interactions which may be expected to vary significantly with heliospheric latitude is supplied by stream-stream interactions. The solar wind originates from different regions of the solar surface, and streams of different density and velocity are present in the heliosphere. Near the ecliptic plane, due to the rotation of the Sun, the faster streams tend to catch up with and overtake the slower streams, with the subsequent formation of a corotating interaction region. Beyond the Earth's orbit, as the interplanetary magnetic-field spiral becomes tighter, a discontinuity develops, flanked by a pair of shocks, the region between the shocks being highly turbulent. At high latitudes the different streams slip past each other, and instabilities driven by velocity shear will develop.

Transient phenomena are also observed in the solar wind. For example, coronal mass-ejections (CMEs) appear to be the driving force behind energetic processes in the lower solar atmosphere. They cause nearly 90% of large geomagnetic storms. MHD fast, intermediate, and slow shock waves are all important in driving the coronal material in front of a CME. High above the ecliptic where the magnetic field may be nearly radial, these shocks will propagate predominantly parallel to the magnetic field, and their study is important to learn how they can accelerate charged particles to high energies and whether they contribute to solar-wind heating.

The type II radio bursts mentioned above are associated with the interaction of electrons accelerated at interplanetary shock waves with the ambient plasma, but the detailed mechanism of the interaction is not understood. The type III bursts result from the nonlinear evolution of the electron-beam plasma instability and the subsequent generation of electromagnetic radiation. There are still many aspects of the theory which remain to be worked out. For instance, we do not understand how the type III intensity varies with frequency or time. Some nonlinear theories predict the existence of intense localized packets of plasma waves called *solitons* which are typically a hundred or so Debye lengths in extent (Gurnett *et al.* 1981). Such events have not yet been observed, except perhaps in the vicinity of the Jovian bow shock. However, few spacecraft to date have had instrumentation with adequate frequency and time resolution to detect them.

Measurements of the quasi-thermal plasma-wave noise spectrum (the so-called plasma line) contribute considerable information about the distribution function of the electrons over short time scales as has been well demonstrated by results at the ISEE-3/ICE mission in the solar wind (Hoang *et al.* 1980) and at the comet Giacobinni-Zinner (Meyer-Vernet *et al.* 1986).

The different kinds of waves interacting with particles must be identified and a complete identification of these modes requires measurements of all their field components, electric and magnetic. It also requires knowledge of their frequencies as compared to characteristic frequencies of the plasma (Fig. 2), the most important of these being the plasma frequency, which should be determined as accurately as possible. A sounder was added to the URAP payload because of the accuracy and stability of this technique for determining ambient electron density, even in the presence of intense wave instabilities around the plasma frequency like the so-called upstream waves in the solar wind (Etcheto & Faucheux 1984).

The time rate of change of the intensity and spectrum of the various phenomena observed will be widely different. Since the bit rate is very limited, it is necessary to provide a selection of compromises between frequency and time resolution. Solitons, lasting only a few milliseconds or less will not be described with high frequency resolution; however, the relatively slowly varying quasi-thermal plasma-wave spectrum does require high-frequency resolution. Figure 3 shows the frequency coverage of the Unified Radio and Plasma Wave instruments. The distribution of the Radio Receiver (RAR) frequencies is selectable by telecommand. The ranges of the Fast Envelope Sampler (FES) are shown with solid and dashed lines; several sets of frequency bands can be chosen by telecommand, and frequency resolution can be traded against time resolution. The two Waveform-Analyzers compute digitally the spectrum in the two bands, ($< 10$ Hz and $> 10$ Hz) as shown.

Although the URAP instrumentation was designed primarily for solar wind studies, it will nevertheless be possible to make interesting observations of Jupiter. As the spacecraft approaches Jupiter, the direction, angular size, and full polarization state (all four Stokes parameters), averaged over 12 sec, of hectometer and kilometer wavelengths of the Jovian radio emission will be obtained for the first time. The intensity of the radiation is believed to be latitude dependent. Most of Jupiter's high frequency emissions are thought to originate on auroral field lines and even some of the kilometric radiation may originate there. In addition to the high latitude auroral zones, another possible source location of the kilometric radiation is the Io torus in the magnetic equatorial plane (Jones & Leblanc 1986) where a multitude of plasma waves are present. Narrow band electrostatic emissions near the upper hybrid resonance and at half integer harmonics of the electron gyro frequency have been observed in the regions of enhanced density of the Io torus. Ulysses, with its high inclination orbit passing through the Io torus, will determine the latitude distributions of these emissions. As Ulysses is a spinning spacecraft, an indication of the polarization of these different types of plasma waves will be obtained. It will be the first spacecraft to make magnetic-wave measurements near Jupiter and the first spacecraft to investigate the high-latitude Jovian magnetopause, magnetosheath, and bow shock. Whistler mode waves have been observed by Voyager in the equatorial region of the Jovian magnetosphere, in the vicinity of the Io torus. The Ulysses trajectory will allow measurements off equator, where those waves are expected to be left-handed, the polarization reversal being due to the presence of a multi-ion plasma. These left-handed waves are considered to be responsible for the EUV aurorae observed at the foot of Io torus field lines (Gurnett & Goertz 1983, Thorne & Moses 1983). The Ulysses outbound trajectory will allow the first exploration of the duskside Jovian magnetosphere (the Pioneer and Voyager spacecraft left Jupiter on its morningside).

## 2. Instrument description.

This section contains considerable detailed information about the sensors and the electronic processing of the URAP instruments. Table 1 is a summary of the most important instrument characteristics for those who do not need a detailed account of the electronics. The various tables in this section contain specific information on parameters such as frequency channels, sensitivities, etc., while Figure 4 shows the overall sensitivity, as a function of frequency, of the instruments.

### 2.1. ANTENNAS AND PREAMPLIFIERS.

### 2.1.1. *Electric field antennas.*

The spacecraft-supplied antenna mechanisms used by the URAP experiment consist of two systems: 1) a pair of wire booms each 35 meters long which form a dipole in the spacecraft spin-plane ($+X$ and $-X$ axes). The elements are made of beryllium-copper tape 5 mm wide and 0.04 mm thick (approximately equivalent to a tube of 2.2 mm diameter) and 2) an axial boom which forms a 7.5 meter monopole antenna along the spin-axis ($-Z$) of the spacecraft. This element is made from a pre-stressed coilable beryllium-copper tube with a complex cross-sectional diameter (see Fig. 18). Low stray capacitance and good EMC characteristics of the deployer mechanisms were design goals.

### 2.1.2. *Electric field preamplifiers.*

Three electric field preamplifier boxes, situated immediately at the foot of each antenna mechanism, are shared by the radio and the plasma wave components of the experiment. The plasma wave preamplifiers cover the range from DC to the highest frequency of the Fast Envelope Sampler, 60 kHz. The dynamic range is from 2 microvolts to several volts. The input impedance consists of a 1000 Mohm resistor bypassed by a 10 pF capacitor. The input and feedback capacitors stabilize the gain in the upper frequency range and suppress high frequency noise. Voltage gain is of the order of unity for frequencies $f >>$ 16 Hz. The DC and very low frequency gains are less (1/4 for $\pm X$ and 1/10 for $Z$), for large signal handling capability. Two relays are included so that a calibration signal (both relays closed) can be applied directly to the input. With one of the relays open the same signal will be applied through a large impedance to measure the antenna impedance.

The Radio Astronomy Receiver preamplifiers cover the frequency range of 1 kHz to 1 MHz. Very low noise JFET input stages provide a high sensitivity. Typical figures for one preamplifier are shown in Table 2.

The input impedance is 27 pF in series with 100 Mohm to ground. The voltage gains are + 18 dB for $\pm X$ and + 26.6 dB for $Z$ at 50 kHz. The 3dB bandpass is 2.5 kHz to 300 kHz and a roll-off at $-6$ dB/octave above that frequency has been implemented because both the natural background and the antenna efficiency increase.

The radio preamplifiers contain 3 relays for a transmit/antitransmit emission-reception switch (Sounder), an internal calibration with both current and voltage sources for impedance and gain measurements, and a 20 dB commandable attenuator for overload protection during the Jupiter flyby.

### 2.1.3. *Magnetic field antennas.*

The two-axis magnetic field sensors (search coils) are located on the spacecraft deployable "radial" boom, 2.05 meters from the spacecraft. The field components measured are $B_y$, along the direction of the boom, and $B_z$ parallel to the spacecraft spin-axis. Each sensor consists of a main winding with a large number of turns on a high permeability rod with a smaller feedback winding. The rod is made of thin layers of ferromagnetic material. The two sensors are identical and operate on the principle of flux-feedback. The resonant frequency of the main winding is within the bandwidth of interest (0.1-500Hz) and its response alone is far from flat. However the response is flattened by re-injecting a feedback field in opposition to the incident field into the secondary winding. This secondary winding is also used as a calibration loop when it is connected to a special calibration signal source.

### 2.1.4. *Magnetic field preamplifiers.*

This unit includes the two low-noise preamplifiers and feedback networks plus circuitry for the de-magnetization of the sensors and filters for the heater power lines. The purpose of the de-magnetization circuit was to reduce in flight any remnant induction of the sensors incurred before or during launch. This was to be achieved by applying a large decaying sine wave to the main windings of the sensors. In-Flight measurements by the DC magnetometer team have indicated that de-magnetization was not required.

Measurements of the noise level of the search coil and preamplifiers were made in flight just after experiment turn on. They show the sensor sensitivity to be as good as deduced from the ground measurements in a quiet site. The combined parameters for the antennas and preamplifiers are shown in Table 3.

### 2.2. RECEIVERS AND SOUNDER.

The URAP experiment is a complex instrument consisting of many electronic subsystems. Other than the sensors and their preamplifiers, there are two stacks of boxes containing the Radio Astronomy and Plasma Receivers, the Waveform Analyzer which does signal processing of the low frequency (<500 Hz) data and of the Sounder data, the Radio AstronomyReceiver programmer, and the common power converter of the instrument. The overall block diagram in Figure 5 shows the interconnections and relations between the various subsystems. The Fast Envelope Sampler is shown as part of the Plasma Frequency Receiver because that is where it is physically located. The Sounder is distributed functionally and physically between the Radio Astronomy Receiver and the microprocessors of the Waveform Analyzer, all of which relinquish their normal function during periods of sounding. The on-board internal calibration cycle of the instrument will be discussed at the end of this chapter.

### 2.2.1. *Principles of direction finding and polarization determination with the radio astronomy receivers.*

To determine the different physical parameters (direction, angular dimension, intensity and polarization) of a radio source radiating at hectometer or kilometer wavelengths, the radio astronomy experiment uses cross-correlation of the outputs from the spin-plane dipole and the spin-axis monopole (Manning & Fainberg, 1980). The relevant phase shift $\delta$ between the preamplifiers driven by the two antenna systems determines the ellipticity of the antenna polarization: if $\delta = 0°$ the polarization is linear, equivalent to a dipole tilted with respect to the spin-axis. The complete measurement of the source polarization requires use of two values of $\delta$ (ideally 0° and 90°). Due to telemetry limitations measurements of the circular polarization with two values of $\delta$ are performed only at high bit rate (1024 bps). Linear polarization measurements can be performed at lower bit rates.

In order to determine the absolute calibration of the radio data, it is necessary to know accurately the antenna effective capacitance and electrical length, as well as the input impedances and receiver gains. Although the latter can be accurately measured on the ground, the antenna characteristics are more difficult to determine. The characteristics of the monopole antenna, which is electrically tilted with respect to the spacecraft spin axis due to currents on the spacecraft body, can best be determined in flight (Fainberg *et al.*, 1985). A method was, therefore, devised to determine the electrical tilt and effective length of the monopole antenna by fitting the synthetic antenna response to intense type III sources at high frequencies. Model simulations showed that the most accurate values would be obtained early in the mission when the solar aspect angle was greatest. The best estimate derived for the electrical tilt of the $Z$-antenna is about 15° from the spin axis, with an azimuth of about + 90° from the $+X$ antenna. The effective electrical length was found to be about 3.5 m.

### 2.2.2. *The radio Astronomy receivers (RAR).*

The radio receivers consist of four superheterodyne receivers whose frequency stepping is programmed in ROM memory and controlled by telecommand. Two receivers, $Z_{\rm L}$ and $Z_{\rm H}$, are connected to the spin-axis ($Z$) preamplifier; the two others, $S_{\rm L}$ and $S_{\rm H}$, are connected to the combination of the signals from the spin-plane ($\pm X$) preamplifiers and the $Z$ preamplifier to form the electronically synthesized tilted dipole. In each case, one receiver is tuned to low frequencies (1.25-48.5 kHz), and the other to high frequencies (52-940 kHz).

The scanning of the two low frequency receivers $Z_{\rm L}$ and $S_{\rm L}$ is controlled by a synthesizer (VCO) which delivers one of 64 programmable local-oscillator frequencies between 433.5 and 480.75 kHz. The intermediate frequency (IF) amplifier operates at 432.25 kHz. It has a dynamic range of about 70 dB and a bandwidth of 750 Hz. The possible low band frequencies are given by

$$f_{\rm L}({\rm kHz}) = 1.25 + (0.75)(n-1)$$

where $n$ is an integer from 1 to 64.

The frequency of the two high frequency receivers is determined by selecting 1 out of 12 high frequency crystal local oscillators (XCO's). The possible high band receiving frequencies, $f_{\rm h}$, are shown in Table 4. The IF amplifier frequency is 10.7 MHz, the dynamic range about 70 dB, and the bandwidth 3 kHz.

The summation of the $\pm X$ and $Z$ signals is done at the output of the mixers of the $S$ receivers. It is possible to interrupt the summation by telecommand or when sounding. The circular polarization measurement is achieved by introducing a 90 degree phase shift on one of the signals at this summation point.

The normal mode of operation is adapted to the time/frequency characteristics of solar radio bursts. The duration of these events varies with the observation frequency. Near 1 MHz, the duration is of the order of a few minutes; below 100 kHz, the events may continue for hours. Optimum resolution of these events requires a non-linear frequency sweep of the receivers. A second constraint is that at least 8 samples should be made of the incoming signal during one spin-period at each observation frequency. These constraints have imposed an observation scheme where, during one 12-second period (~ one spin period), 8 samples at three different frequencies are taken with the high frequency receiver and 12 samples at one frequency are taken with the low frequency receiver. A number of different "programs" are stored in ROM memory which permit cycling through lists of frequencies which in general favor the higher frequencies. The various lists depend on models of the observable phenomena and will be changed during the life of the mission.

The low frequency receivers can also work in a linear sweep mode in which they sweep all 64 frequencies. This mode is used in particular for the plasma line measurements.

### 2.2.3. *Plasma frequency receiver (PFR).*

The Plasma Frequency Receiver is intended to monitor the wide spectrum of plasma phenomena with constant frequency coverage, large dynamic range, and good frequency resolution. Two such receivers are supplied, one for $E_x$ and one for $E_z$. The frequency range, 0.57 to 35 kHz, is covered in 32 logarithmic frequency steps, with a corresponding separation of 14%. Table 5 lists the 32 frequency channels. The threshold sensitivity is approximately 2 $\mu v$ per channel. Receiver tuning is controlled by an RCA 1802 microprocessor, and is done in either fast scan or slow scan, selected by ground command. In the nominal fast scan, the receivers are swept through all their 32 frequency steps twice in each frame. The time, $\Delta t$, that the receiver stays in one tuning position in high bit rate is given by:

$$\Delta f \; \Delta t \sim 10$$

The bandwidth, $\Delta f = f/4Q$ (where $Q$ is the quality factor), is about 14% of the center frequency and it may easily be shown that this procedure allows a full frequency scan in $\sim$ 0.5 sec. There is not sufficient telemetry to send full scans at this rate so 32 scans are averaged, frequency by frequency, and the maximum or peak signal at each frequency of these 32 scans in the $E_x$ receiver is also kept. Three amplitudes ($E_x$ average, $E_x$ peak, and $E_z$ average) at each of two frequencies, are telemetered in each frame, so a full scan is read out in 16 frames. A frequency scan is started shortly after a frame pulse ($\sim$ 10 msec) and the second frequency scan immediately follows the first. Since a full readout in fast scan has been averaged over 16 frames, the directional variation of the signal has been averaged out. In the slow scan mode directional information is preserved. The frequency is stepped only twice per frame. In each half-frame, 32 measurements of the signal at the same frequency are made and averaged, and the peak found, as before. In slow scan, the receiver stays in one tuning position for 14.7 msec, independent of frequency. The telemetry is unchanged. For each half-frame, the data to be telemetered are 3 eight-bit digital words, for $E_x$ (average), $E_z$ (average), $E_x$ (maximum). It is also possible, in the slow scan mode, to bypass the frequency stepping and remain locked on a fixed frequency. Each word represents the signal amplitude in 1/2 dB steps above threshold, so that the dynamic range is approximately 128 dB.

### 2.2.4. *Waveform analyser (WFA).*

The Waveform Analyzer or FFT-DPU (Fast Fourier Transform Data Processing Unit) provides spectral analysis in the frequency range from 0.08 to 448 Hz of signals received from the plasma wave and magnetic preamplifiers. The spectral analysis is performed separately for frequencies below 10 Hz and between 10 Hz and 448 Hz.

The > 10 Hz processing is done by three microprocessors, each dedicated to one of the $E_x$, $B_y$, and the selected $B_z$ or $E_z$ sources. The information is band pass filtered, and passed through a gain ranger from ×1 to ×4096 in ×8 steps. The gain range is used to create an exponent and the analog-to-digital conversion of the ranged data is used to create a mantissa from which the data is processed in floating point. The sample rate for this data is 1.792 kHz. Spectra are produced and are summed for 2 formats of the spacecraft telemetry. This 2-format cycle is the normal DPU major cycle. Table 6 shows the 12 log-spaced band centers. The amplitudes at the centers of the twelve bands are determined using a modified Walsh transform, giving a bandwidth of 25%. A triangular window is also applied to increase side-lobe rejection. The highest band (448 Hz) is obtained directly; five other bands are obtained by iterative use of an averaging algorithm to create bands which are factors of two lower in frequency than the highest band. The next to highest band is obtained after application of another algorithm which creates a band (229 Hz) equal to two thirds of the highest band; the remaining five bands are obtained by further use of the averaging algorithm. A spectrum is taken for each octant of spacecraft rotation. There are generally 5 or 10 rotations during the 2-format major cycle. One set of data obtained, called the averaged data is the sum of these 5 or 10 spectra per octant, which are then grouped together by opposite octants, giving Four 12-point spectra per antenna. Another set of data, called peak data is obtained by taking the largest values recorded for the $E_x$ channel for each frequency and octant, and the values of $B_y$ and $B_z$ or $E_z$ taken at the same time. A third set of data, is a measurement of the phase between the $E_x$ channel and the two others at the same time that the peak measurement was made. The resolution is 1/16th of a revolution, or 22.5 degrees. This gives an indication of the direction of arrival of the largest incoming signals.

Signals for the < 10 Hz processing are obtained from the $E_x$ and the selected $B_y$ or $B_z$ sources which have been low-pass filtered and converted with a 10-bit analog-to-digital converter. The sample rate of the signals is 256 times per spin of the spacecraft, and a spectrum is produced every 16 telemetry frames, representing one spin. The same averaging algorithm is used to obtain the logarithmically-spaced bands. Table 7 shows the 12 band centers below 10 Hz band.

The DPU is reconfigured when the sounder experiment operates. At these times, WFA data are not obtained. Section 2.2.7 describes sounder operation.

### 2.2.5. *DC voltage measurements.*

DC voltage measurements are made using the plasma wave preamplifiers and some signal conditioning within the same box and are digitized by the Spacecraft Data Handling System. The differential output of the $X$ preamplifiers is digitized to 10 bits of which 8 are selectable by telecommand. There is also a $\times 0.5/\times 8$ gain switch in the PFR. These options increase the dynamic range of the measurement. This scheme is however not sufficient for the $Z$ DC measurements because of the anticipated large floating potential variations. An automatic insertion of an offset voltage (in 5 Volt steps) has been implemented. The DPU decides each one-half format whether the signal it is receiving is going off-scale and if so modifies the offset command it is sending to the PFR. This state is also sent to telemetry. The resolution of the $X$ DC measurements is either 2.5 or 40 mV and that of the $Z$ DC measurements is approximately 50 mV. The full scale measurable amplitudes are $\pm$ 5 Volts for $X$ and $+$ 15 to $-75$ Volts for $Z$. There are two sets of measurements made for $X$ DC and $Z$ DC each, fixed and scan. Fixed means that the samples are made at fixed angles with respect to the spacecraft rotation and scan means that the sample angle is changed each time by an amount such that after 512 samples each angle (512th of a spin) has been seen. This permits a reconstitution of the average field around the spacecraft. The voltage on the $+X$ preamplifier output is also sent directly to the analog telemetry of the spacecraft. The possible full-scale amplitude at the preamplifier input of this non-differential measurement is about $\pm$ 20 Volts.

### 2.2.6. *Fast envelope sampler (FES).*

The solar wind and the unstable plasmas near Jupiter exhibit many transient, rapidly varying phenomena. The purpose of the Fast Envelope Sampler is to capture such rapidly varying phenomena, at sample rates up to the order of one sample per millisecond, and store them in a memory for later telemetry. Larger events will replace smaller events in this memory, so that the telemetered event will be the largest in the interval since the last readout. The FES contains commandable filters for the isolation of one phenomenon in the presence of others, but otherwise has no frequency resolution, and only samples the envelope of the detected signal. Two filter channels (Hi and Lo) are used concurrently. The memory length is 48 $\times$ 1024 bits. A memory load will be triggered by a large signal. However, it is also desired to save some data from the period immediately preceding the large signal, i.e., the peak signal should appear roughly in the middle of the stored data sequence. This implies that a section of the memory must be used to store data waiting for a trigger. These data will be stored temporarily and will be erased if no trigger comes. In addition, an equal part of the memory must be used as an output buffer to telemetry. Consequently, the length of an event is one-sixth the total memory length as one-third must be used as a buffer to telemetry and another part is to be used for transient storage of data for which a decision has not yet been made, and half the memory is devoted to each frequency channel. In order to save space, the data are 6-bit words, with one step equalling 1 dB. Selection of the signal inputs for the two sections of the FES, namely, the high frequency filter and the low frequency filter, can be made either under program control or by telecommand. The commandable frequency bands are given in Table 8.

The sampling period is selectable as follows: one sample per 1.12 msec, 4.46 msec, 17.8 msec, or 71.4 msec. Even at the fastest sampling rate, the sampling rate would not be sufficient to resolve Langmuir solitons which may have a peak as short as one-half cycle of a 20 kHz wave, i.e., be only 25 $\mu$sec long. Therefore, the detector for the FES consists of a full-wave rectifier followed by a peak detector so that the peak signal amplitude in each sampling interval is stored. In order to extend the dynamic range of the system, a 32 dB attenuator is switched into the signal stream whenever the signal rises to saturation. It remains connected for the remainder of the event cycle and is switched out again when the output buffer has been emptied and selection of a new event is started. The maximum signal per format seen in each channel is kept and telemetered in the following format.

### 2.2.7. *Sounder.*

The sounder, which was incorporated late in the planning phase of the experiment, was designed around use of the low frequency radio receiver. The only specific hardware items added were two simple transmitters, small additions to the radio receivers, and extra ROM for the microprocessors. Operation of the sounder is controlled by the DPU. When, according to the duty cycle, it is time to sound, it sends a signal to the low frequency receiver which begins stepping systematically, once every 2 sec, through each of its frequency steps so that in 128 sec the frequency range 1.25-48.5 kHz is swept in 64 contiguous 750 Hz bands. Meanwhile, relays switch transmitter circuitry in parallel with the preamplifier inputs. During this cycle the DPU controls the sounder pulse transmissions and uses a special output of this receiver to make a finer frequency analysis. The sequence of operations on each frequency step is a follows. One second after switching from the previous frequency the receiver clamps its gain (AGC level) according to the new background level. Following this the microprocessor sends a gating signal to the radio receiver for the transmission. During this gating signal the receiver sends pulses at the desired frequency to transmitters in the preamp boxes. These transmitters alternately apply 30 Volts directly to the $+X$ and $-X$ antenna connections. The duration of the envelope of the transmitted pulses is 1.33 msec. The inputs to the preamplifiers are simultaneously short-circuited to avoid saturation of the receivers. The receiver output waveform is transposed to the band 1000 ± 375 Hz and sent to the DPU. The analysis performed by the FFT-DPU is analogous to a 64-point Fourier analysis taken during 15.6 msec intervals of the incoming signal. Each of three microprocessors successively takes 128 samples of the signal at a sampling rate of 8192 Hz. A modified Walsh transform, which involves only additions and subtractions, is used. The complete transform is not computed, but only the "Fourier" power coefficients 11 to 22, which correspond to 12 frequencies separated by 64 Hertz centered around 1024 Hz. To adapt its operation to the characteristics of the ambient plasma and to the available bit rate, the sounder has several modes of operation. Changes fall into two broad categories: changes in the sequence of pulse activity and changes in the on-board data analysis.

### 2.3. ON-BOARD CALIBRATIONS.

An internal calibration cycle is programmed automatically at commandable intervals provide to a very complete checkout of the experiment. The RAR on the one hand and the PFR and the WFA on the other hand have their own calibration cycles which can be initiated independently, but normally the DPU triggers the calibration of the two sequentially. The internal calibration cycle also provides some rudimentary measurements of the antenna impedances.

### 2.4. POWER CONVERTER.

The power to the entire URAP experiment is supplied by a common power converter module. The design is such that a single-point failure cannot incapacitate the entire experiment. The unit is remarkable for its very low level of generated interference which has been accomplished by close control of rise-times, transformer shielding, grounding and layout. The problem was made much more difficult by the large number of output voltages, which were implemented in order to avoid cross-subsystem interference by supplying separate secondary power for the RAR, the PFR, the WFA, and especially the radio and the plasma preamplifiers.

## 3. Preliminary results.

In this section, some preliminary observations of plasma and radio waves from the URAP instruments are presented to demonstrate how well the instrument is functioning and to provide the reader with a first-hand look at the types of phenomena and methods of presentation which will be used in future publications. These results are intended only to demonstrate the operation of the experiment and not as definitive scientific results. The instruments primarily involved in the observations are referred to in parentheses in the section titles.

### 3.1. TRACKING RADIO SOURCES (RAR).

The synthetic antenna responses and the Z-axis antenna response to a remote radio source vary in a predictable way as the spacecraft rotates about its spin axis. For a uniform circular source distribution, analytic expressions have been derived which relate the various antenna responses to the antenna and source characteristics (Manning & Fainberg 1980; Fainberg *et al.* 1985). Figure 6 shows the three antenna responses at 540 kHz for a type III event occurring on December 9, 1990 at 06:20 UT. Figures 6a and 6b correspond to the response of the synthetic antenna during one spacecraft rotation period, when phase shifts of 0° and 90°, respectively, are introduced between the inputs from the $S$ and $Z$ antennas. Figure 6c shows the response from the $Z$-axis antenna alone. It is modulated because the $Z$-monopole antenna is electrically tilted with respect to the spacecraft spin axis. The error bars reflect the magnitude of the noise in the receivers. The source parameters, derived by fitting the analytical antenna expressions to the data shown in Figure 6, suggest a radio source with an angular radius of 25°, and radio centroid located about 4° to the west of the spacecraft/Sun line and about 0.5° above the ecliptic plane. These source parameters are reasonable for a radio source originating on the Sun to the west of the spacecraft-Sun line. In this initial analysis, it was assumed that this type III burst is not polarized. By repeating this fitting procedure at other observing frequencies, and assuming a frequency-distance scale, the type III radio burst can, in principle, be tracked through the interplanetary medium.

### 3.2. AN EXAMPLE OF "UNIFIED RADIO & PLASMA WAVE OBSERVATIONS" -SOLAR RADIO BURST AND ASSOCIATED LANGMUIR WAVES (RAR, PFR, AND FES).

Solar radio emissions are produced by interactions of suprathermal electron beams with the ambient interplanetary plasma. The precise mechanisms by which the beam electrons excite the plasma wave instabilities and by which these plasma wave-wave and wave-particle interactions produce the radio emissions is not well established. By incorporating both radio wave and plasma wave instruments in the same experiment, the Ulysses URAP experiment offers a unique opportunity for studying the relationship between the radio emissions and their associated plasma wave phenomena.

As an illustration of such a unified approach, we show in Figure 7 some URAP observations for December 10, 1990. The dynamic spectrum shows a number of kilometric type III radio bursts. The radio emissions from these bursts extend from the highest RAR frequency of 940 kHz, corresponding to the radio source lying near the Sun, often down to radio frequencies below 30 kHz, corresponding to the radio source lying in the interplanetary medium far from the Sun.

The top twelve frequencies, from 940 kHz to 52 kHz, are from the high-band receiver, with 3 kHz bandwidth, and are plotted on an approximately logarithmic scale, with the highest frequency on the top. The intensity of each pixel represents the maximum values of the observed data over 128 seconds. Average background values were determined for each frequency and subtracted from the raw data. The dynamic range displayed is approximately 25 dB. The darkness of the shading of the data pixels increases with increasing intensity. At the time of this data, the high frequency receiver was in synthetic antenna mode.

The low frequency receiver, corresponding to frequencies from 1.25 kHz to 48.5 kHz with a bandwidth of 750 Hz, is in linear sweep mode and the frequency scale is linear, each frequency step corresponding to 0.75 kHz. The low frequency receiver sweeps through the 64 frequencies every 128 seconds. Background values are determined and subtracted as for the high frequency receiver, and the dynamic range displayed for this low frequency receiver data is approximately 25 dB.

An intensity-time plot of the radio data at 940 kHz is shown in Figure 7b. We focus here on two bursts, the first beginning at 7:47 UT and the second beginning at 9:45 UT. Both of these type III bursts are associated with flares from the solar active region, NOAA 6398, which at the time of these observations was located about 50° west of central meridian. A 2B flare, whose maximum intensity occurred at 7:55 UT, is associated with the first burst; an SF flare, whose maximum intensity occurred at 9:43 UT, with the second burst. Metric type III radio bursts were also observed at these times.

Since at the time of these observations, Ulysses was at 1.35 AU and the Earth-Sun Spacecraft angle was 8° (its heliocentric latitude was 0.8°), this flare site lies about 42° to the west of the Ulysses spacecraft-Sun line. Assuming that the type III electrons are injected into the interplanetary medium over a typical solar longitudinal angular width of 60° to 70°, the magnetic field lines from this active region are expected to be well connected to the spacecraft. The spacecraft should, therefore, lie within the beam of suprathermal electrons, which produced the observed kilometric type III burst. Consequently, when the energetic electrons arrive, Langmuir waves are expected to be excited in the vicinity of the spacecraft due to the formation of a bump-on-tail in the electron parallel velocity distribution (Lin *et al.* 1981).

The 21 kHz PFR data from 7:00 UT to 11:00 UT are also shown in Figure 7b. At a given frequency, the time resolution is 16 seconds. The vertical scale, which corresponds to the amplitude of the plasma waves, is in telemetry units. Burst of plasma waves are observed at about 8:17 UT and 10:13 UT with a maximum intensity at about 20 kHz. As seen in Figure 7a this is consistent with the quasi-thermal noise spectral line (see Sect. 3.4) which indicates a plasma frequency of about 20 kHz in the vicinity of the spacecraft.

The time difference of 116 minutes between the two plasma wave events that are observed at the spacecraft is very nearly equal to the time difference between the onset of the two type III/flare events that are observed near the Sun. This strongly suggests a one-to-one correspondance. (The type III burst beginning at 9:58 UT may be associated with the plasma waves observed about 10:20 UT). Assuming a spiral path length to the spacecraft of 1.68 AU, these observed plasma wave onset times imply electron exciter transit speeds of c/2 for both bursts.

These exciter speeds are similar to those previously obtained for type III radio bursts (Fainberg & Stone 1970). More recently, Dulk *et al.* (1987) have found much lower electron exciter speeds, of the order of c/10. One can obtain such a speed by associating the *in-situ* plasma waves at 10:13 UT with the type III burst at 7:50 UT. One then has the difficulty of finding an association for the *in-situ* plasma waves observed at 8:17 UT. Perhaps they can be associated with a very weak type III burst at 6:00 UT. Since there is no flare associated with this latter burst, however, we cannot determine if it occurs in a region that is well connected to the spacecraft. Although, with these data we cannot rule out this alternative interpretation, we believe that it is less likely.

Finally, Figure 8 shows a rapidly varying Langmuir event which was recorded in the high-frequency, 6 to 60 kHz band, of the FES at 10:12:36.5 UT, i.e., at the onset of the plasma waves. No event was observed in the low-frequency, 600 Hz to 6 kHz band, of the FES at this time. In the figure, time between samples is 1.12 msec, so that the entire sweep of the 1024 data points corresponds to 1.15 seconds. After the large event at the center, at 10:12:36.5 UT, the 32 dB attenuator was switched on for the remainder of the sweep. The vertical scale, which corresponds to the amplitude of the signal, is in telemetry units. The duration of the triggering central group of events is about 70 msec. The duration of the central spike is about 15 msec.

This sequence of observations, from remote sensing of radio waves to observed *in-situ* plasma phenomena, illustrates how radio wave and plasma wave phenomena, associated with energetic solar activity, will be correlated and studied using the URAP experiment.

### 3.3. PLANETARY EMISSIONS (RAR).

#### 3.3.1. *Earth.*

The most intense planetary emission observed thus far with URAP is auroral kilometric radiation, or AKR, which originates at high latitudes on the nightside in the Earth's auroral regions. Figure 9 shows an example of AKR seen in the range from 81 to 387 kHz. As is apparent in the figure, the AKR, like most planetary emission, is highly impulsive, especially when compared with the solar emission in the same frequency range. The episodes of AKR emission tend to occur approximately every 12 hours, corresponding to the times when the Earth's magnetic polar regions are tilted in the direction of the spacecraft. AKR is believed to result from an electron cyclotron maser process involving a wave-particle interaction on auroral magnetic field lines. The result is intense, predominantly extraordinary ($R_X$) mode radiation. Given the high sensitivity of the URAP system, we estimate that we should be able to detect AKR over the duration of the mission, including the Jupiter encounter interval during times when Jupiter is inactive.

#### 3.3.2. *Jupiter.*

Jupiter is known to be intrinsically the most powerful emitter of planetary radio waves in the solar system, on KOM to DAM wavelengths (except in the range ~ 100-400 kHz, where Saturn's kilometer emission is more intense on the average (Zarka, 1991)). Four components of Jupiter's radio radiation can be distinguished (Carr *et al.*, 1983; Zarka, 1991). With increasing frequencies: (i) a narrowband kilometer emission (n-KOM), about 100 kHz, possibly originating from the vicinity of Io's plasma torus; (ii) a broadband kilometer component (b-KOM), extending from ~ 20 kHz to 1 MHz, emitted from the outer edge of Io's torus or from an auroral source spread along a high latitude set of (open) field lines; (iii) an auroral emission on hectometer (HOM) to decameter (DAM) wavelengths, in the range from ~ 100 kHz to > 20 MHz with a peak about 1-2 MHz, coming from high latitude ($L >> 6$) auroral regions, analogous to the other auroral planetary radio emissions; and (iv) an additional DAM component, peaking about 10-15 MHz, thought to be generated near the footprint of Io's torus.

With URAP, we have observed two of these four components. HOM emission has been observed by the radio astronomy receiver (RAR). Like AKR and the other auroral planetary radio emissions, HOM is emitted in the $R_X$ mode. Its lower frequency cutoff, probably about a few tens of kHz, has not yet been identified due to the distance from Jupiter. The precise origin of the HOM is not well known, however the URAP direction-finding capability should allow us to pin-point the source of HOM during the close approach to Jupiter.

At lower frequencies (Fig. 9), we have detected the b-KOM emission, which was discovered by Voyager (Warwick *et al.* 1979; Scarf *et al.* 1979). At this early stage of analysis, several things appear to be unique about the URAP observations of b-KOM: first, the b-KOM has been detected much farther from the planet than was the case with Voyager; this is not only due to the greatly improved sensitivity, but also to the striking change in the relative intensities of b-KOM and HOM emissions, with respect to the previous Voyager observations; HOM was detected at ~ 1 MHz practically at Voyager's launch (at 4 A.U. from Jupiter) while b-KOM was discovered several months later (at 2 A.U. from Jupiter); conversely, the b-KOM emission is undoubtedly the most intense component in the Ulysses data. Second, because the low-band portion of the RAR has vastly superior frequency resolution compared to Voyager, the low frequency end of b-KOM is well-defined for the first time. Finally, from the Voyager spacecraft, usually only the northern b-KOM was observed per rotation of the planet because the latitude of both Voyagers relative to Jupiter's equator was always > 3deg. That is, the observations from Voyager were predominantly over the northern jovigraphic hemisphere. However, Ulysses at present is approaching Jupiter very nearly in the plane of the jovigraphic equator. Near closest approach to Jupiter (see Fig. 10), during the planetary swing-by, the URAP direction-finding will also allow us to distinguish between the two alternate source locations of b-KOM, and hopefully resolve for the first time the question of the origin of the b-KOM. If generated on auroral field lines, near the local electronic gyrofrequency, the b-KOM, due to its frequency range, would come from a source located as far as 6-7 $R_{\rm J}$ from the center of the planet, thus source crossing by Ulysses may occur during the Jupiter flyby.

### 3.4. THERMAL NOISE (RAR).

The dynamic spectra obtained with the long $X$-dipole (see for example Fig. 1) show the time evolution of the plasma frequency line. This emission is due to the quasi-thermal noise of the plasma, i.e., the voltage induced on the antenna by the random motion of the ambient electrons. This motion excites plasma waves near the plasma frequency $f_{\rm p}$. Because these waves have a frequency-dependent wavelength longer than the plasma Debye length $L_{\rm D}$, a good detection of the plasma frequency requires an antenna of length $L$ greater than $L_{\rm D}$. The longer the antenna, the sharper the plasma frequency line; since $L_{\rm D}$ varies as $\sqrt{(T)}/f_{\rm p}$ ($T$ being the electron temperature), $L/L_{\rm D}$ increases with $f_{\rm p}$. This explains why, on the dynamic spectra, the plasma line generally becomes more intense when the plasma frequency increases, and also why it is barely visible on the short axial $Z$-antenna.

This feature allows a quick and fairly accurate measurement of the local electron density to be made without any special processing. In addition, a more complete analysis also gives the temperature and other parameters of the electron distibution function.

The URAP experiment is relatively well suited for this purpose since the receiver is very sensitive and well calibrated, and the $X$ dipole antenna is sufficiently long to be quite free of spacecraft perturbations. Because the antenna length is generally not much longer than $L_D$ in the solar wind, the temperature is not determined precisely (see Meyer-Vernet & Perche 1989). The instrument precision is best when the density is larger than about 10 electrons/cm$^3$ and the temperature smaller than $1 \times 10^5$ K (in which case $L/L_D = 5$) : these conditions will presumably occur when Ulysses passes through the Io torus near Jupiter (see Sittler & Strobel 1987).

Figure 11 shows an example of the spectrum measured by the low-frequency receiver with the long antenna. The thermal noise around the plasma frequency is similar to that observed aboard ISEE-3 in the solar wind (Couturier *et al.* 1981) with two significant differences. First, aboard Ulysses, the frequency resolution is at least 5 times better than on ISEE-3. The time resolution is also much better since, although a complete spectrum is acquired in 128 sec, the plasma line profile is acquired during a much shorter time. Second, since the lowest channel is near 1 kHz, the part of the spectrum below $f_p$ is clearly visible. This noise, which increases at lower frequencies is due to the ion contribution to the thermal noise, Doppler-shifted by the solar wind velocity (Meyer-Vernet *et al.* 1986) and to the shot noise of the plasma electrons collected (and the photo-electrons emitted) by the antenna surface. With the Ulysses $X$-antenna, the latter contribution is expected to dominate because the antenna surface is rather large. For the short axial $Z$-boom, which has a much larger surface, this noise even dominates the plasma line.

In Figure 11, the plotted theoretical spectrum was obtained in the following way. The "thermal" noise at the antenna ports is calculated by describing the electron velocity distribution function with a sum of two Maxwellians ("cold" and "hot", with respective densities $n_c$ and $n_h$ and temperatures $T_c$ and $T_h$). For comparison with the spectrum measured at the receiver ports, we must take into account the receiver gain, which involves the base capacitance and the impedance of the antenna in the plasma. For these preliminary results, the latter values was calculated in an approximate way, which will be refined later.

A fitting of the spectrum gives the four plasma parameters of the electron distribution. One can see that the overall agreement is rather good. We believe that the small discrepancies are not significant, because the calculations are very preliminary. Indeed, the excellent performances of the receiver and the electrical cleanliness of the spacecraft suggest that a comparison of the spectra with the theoretical thermal noise might allow a distinction between distribution functions made of Maxwellians, as frequently assumed for the solar wind and, for instance, "Kappa" distributions (Chateau & Meyer-Vernet 1991).

## 3.5. PLASMA WAVES.

### 3.5.1. *Langmuir Waves and Ion Acoustic-Like Noise (PFR).*

The principal signals seen by the PFR fall into two bands. The first is at the electron plasma frequency. There is a steady signal at the plasma frequency, the thermal line discussed above, which is occasionally and impulsively enhanced by a large factor to give intense bursts at a range of frequencies around the plasma frequency. These bursts are so short that they are most clearly shown in the $E_X$ peak data, sometimes being nearly invisible in the data which have been averaged over 32 samples. The second range is what Gurnett & Frank (1978) have called the ion acoustic range, a range of frequencies from a fraction of a kilohertz up to a few kilohertz. These signals are also very impulsive and show more clearly in the peak data than in the average data. Figure 12 shows a gray scale plot of plasma frequency data for an event on November 17, 1990. Both the impulsive plasma frequency emission and ion acoustic-like emission are shown. Note the clear anti-correlation between these two components. However, the plasma frequency emissions are rarer than the ion acoustic emissions and this period is not typical.

### 3.5.2. *Whistler-like noise (WFA).*

The electromagnetic waves that can be measured by the search coil antennas and analyzed by the Wave Form Analyzer are either ion-cyclotron waves emitted below the proton gyrofrequency (some tens of Hz) or whistler mode waves emitted, below the electron gyro-frequency (some 100 Hz). The latter have been observed mainly in the vicinity of solar wind discontinuities. For example, this can be seen in the case of the discontinuity observed on November 12, 1990. At about 07:00 UT, the plasma line, as measured with the radio receiver, showed that the plasma frequency increased abruptly from slightly less than 20 kHz to about 36 kHz so that the density increased by a factor of four. After that time the density is highly variable. Figure 13 shows the evolution of the magnetic components at four different frequencies, in the range 1.7 to 79 Hz, from 0:600 to 15:00 UT. The wave occurence can be roughly divided into five time intervals that correspond to the cold plasma density evolution. From 06:40 to 08:00 UT, just after the density increase, waves are emitted at rather low frequency, as after 13:00 UT when a new density enhancement is observed. The highest frequencies occur between 10:00 and 12:00 UT, at the time of a plasma density minimum whereas intermediate frequencies correspond to intermediate density values (from 08:00 to 09:00 UT and 12:00 to 13:00 UT). The maximum wave intensity observed during these events is about

200 pT (the larger signal at 06:30 UT is a calibration). Two typical detailed spectra, averaged over 64 seconds of data, are given in Figure 14. One can see that the spectra are rather narrow band.

### 3.5.3. *Whistler-like Noise (FES).*

An example of whistler-like emission captured by the FES is shown in Figure 15. Note the short time structure of the emission (~msec) which can be observed by this instrument. The high channel is fed by the $E_X$ antenna and is measuring the band from 6 to 60 kHz. The low channel is attached to the $B_Y$ antenna. It will be seen that there is a large signal in the magnetic antenna at about 14 Hz (note that the FES rectifies the signal), which is loosely associated with the intense emissions at the higher frequency. These events are not common and are not randomly distributed in time. Six were observed on December 26, 1990. The most intense signal found so far in the 6 to 60 kHz electric antenna is about 10 mV/m, consistent with that found by Gurnett *et al.* (1978).

## 3.6. DC VOLTAGE MEASUREMENTS.

DC signals refer to measurements of the instantaneous potential or potential difference of the antennas. There are three potentials that are measured: the potential on the $Z$ antenna with respect to the spacecraft ($E_{\mathrm{ZDC}}$), the potential of the $+X$ antenna with respect to the spacecraft ($E_{\mathrm{XAN}}$), and the potential difference between the two $X$ antennas ($E_{\mathrm{XDC}}$).

It is generally expected that the potentials of the antennas will be determined by the balance between photoelectric emission and plasma electron pickup. Since the plasma electron pickup is independent of antenna aspect whereas the photoelectric emission depends on the area presented to the sun, this voltage varies as the antenna turns. The photoelectric potential on the $Z$ antenna after instrument turn-on was surprisingly and unfortunately large and complex. Typical measurements of $E_{\mathrm{ZDC}}$ obtained by accumulation of data during a period of about an hour of $Z$ antenna voltage as a function of rotation angle are shown in Figure 16. It will be seen that the signal has two peaks, that the peak-to-peak variation is greater than one volt and that there is a rapidly varying structure which will give high harmonics of the spacecraft rotation frequency. Part of the cause of these variations, is the peculiar cross section of the antenna (see Fig. 16d) such that it presents a much larger area to the Sun at one rotation phase and a smaller area 90 degrees later. As the Ulysses spin axis turns towards the Sun, the $Z$ antenna should sometimes be completely shadowed from the Sun. Then the antenna no longer has to attract back its photoelectrons so it is driven negative by the solar wind electron flux. On December 22, 1990, the $Z$ antenna was being shadowed by the corners of the spacecraft at 225° and 315°, but not by those on the RTG side at 45° and 135°. The large dip around 90° is due to shadowing by the RTG. By December 26, 1990, the antenna was apparently completely in the spacecraft shadow where the antenna potential is $-9$ to $-12$ volts.

The variation with antenna rotation of the potential on the $X$ antenna ($+E_{\mathrm{XAN}}$) is expected to slowly decrease as Ulysses faces more and more toward the Sun with consequent smaller variation of the area presented to the Sun, as shown in Figure 17. The potential of each monopole is determined by competition between plasma electron pickup and photoemission. To zeroth order, the photoemission has two minima per spin, one when the antenna is pointing at the sun and one when it is pointing away, whereas the electron pickup is isotropic since solar wind electrons have a thermal speed much higher than the solar wind speed. It is desired to measure the electric field in the solar wind which of course also would give rise to one peak per spin. To zeroth order then the photoemission is a common mode effect which cancels out. However, there are two first order effects, namely a photoelectric coupling between the antenna and the illuminated side of the spacecraft and the partial shadowing of the root of the antenna which is facing away from the spacecraft which give rise to one cycle per spin effects. These have always been a problem in electric field measurements. Already by November 12, 1990 the photo effects had decreased sufficiently that effects of changing interplanetary electric field could be seen. Electric field data, corresponding to the density increase period around 07:00 UT already discussed above in paragraph 3.5.2 are shown in Figure 18. Note that this is electric field as obtained from the spin plane antenna and therefore represents only two components of the electric field. It will be seen that the voltage measured on the antenna decreased although the phase did not change by very much. It is believed that the phase is still badly contaminated by the effects discussed above. Nevertheless, this indicates that we will eventually be able to use these measurements for determination of two components of the interplanetary electric field. However, translation of the data in Figure 18 into a genuine electric field must await a careful evaluation of the effects of photoelectric base resistance and other spurious effects.

## 3.7. SOUNDER.

The major purpose of a relaxation sounder is to provide a reliable measure of the local electron plasma density, through the detection of the resonance excited close to the electron plasma frequency. Such instruments have been flown successfully on Earthbound spacecraft (GEOS-1, GEOS-2, ISEE-1, VIKING). ISEE-1 data have shown that this instrument, originally designed to operate in Earth's magnetosphere, works perfectly in the solar wind (Harvey *et al.*, 1979). The relaxation sounder uses the same antenna for both pulse emission and resonance reception. Data gathered soon after instrument turn-on have demonstrated the feasibility of the approach. The sounder design makes use of the very narrow bandwidth of the resonances excited by the sounder. The signal is analyzed on board by the URAP DPU (a modified Walsh transform is used) in order to improve the frequency resolution of the low frequency radio receiver from 750 Hz to 64 Hz, and thus to provide a better signal to noise ratio. The first resonances observed by the URAP sounder were indeed very narrow-band signals. Typically a resonance is seen in two adjacent channels which, with a channel separation of 64 Hz, implies a signal bandwidth of at most 128 Hz. The typical S/N ratio for resonances is 40 dB. Whereas the identification of the electron plasma frequency is complicated by many tens of resonances being observed on a typical sounder spectrum obtained in the Earth's magnetosphere, diagnosis is straight forward in the solar wind where a single resonance is excited. Figure 19 shows a series of resonances on successive sweeps of the sounder, and the variation of the ambient plasma frequency is clearly visible. In this example successive sweeps occurred at intervals of about 20 min. The ease with which the electron density is determined is evident and the precision of the method has been discussed elsewhere (Harvey *et al.* 1979, Trotignon *et al.* 1986). On the third spectrum (9:12 UT), strong natural emission, below 10 kHz, are observed with the very high frequency resolution available from the instruments. There is close correlation between the frequency of the plasma resonance and the profile of the plasma "thermal line" observed by the radio astronomy receiver, but a detailed comparison has not yet been performed.

The sounder is expected to provide a reliable monitor of the solar wind electron density throughout the Ulysses mission. In addition, it will provide unique observations in the Jovian magnetosphere. The instrument will be used to identify the plasma frequency on spectra more complex than those of the solar wind, and to help with the identification of waves, mainly Bernstein modes (Kurth *et al.* 1980, Birmingham *et al.* 1981). It will also allow routine study of these electrostatic emissions with a frequency resolution one hundred times better than that available from the Voyager instruments.

### 3.8. SUMMARY.

The scientific goals, operation of the instrument, and examples of observations with the Unified Radio and Plasma Wave (URAP) investigation have been presented. The instrument will provide the source direction, angular size, and full polarization state of solar type II and III radio bursts, and the Jovian sources including bKOM, nKOM, and HOM. Tracking type III solar bursts as a function of observing frequency will lead to a 3 dimensional "snapshot" out to distances of the order of 1 AU from the Sun, of the large scale magnetic field structure along which the radio burst propagated. Observations of the Jovian sources will provide information on their location and emission process. Both the relaxation sounder and thermal noise "spectroscopy" yield accurate measurements of the local electron density. Thermal noise spectroscopy can provide information on the "hot" and "cold" temperatures and electron densities of a bi-Maxwellian velocity distribution. The radio and plasma wave receivers, which cover the frequency range from DC to 1 MHz, have been able to investigate various wave modes occurring both at interplanetary discontinuities, such as shock waves, and in connection with the suprathermal electron packets responsible for type III radio emissions. Langmuir waves, ion-acoustic like noise, and whistlers have been observed. The Fast Envelope Sampler has observed ~ 1 msec Langmuir wave structures. DC measurements with the antenna systems will be used to measure DC electric fields in the solar wind.

## 4. Acknowledgements.

The French contribution to this experiment has been financed by the Centre National d'Etudes Spatiales. All three French laboratories are associated with the Centre National de la Recherche Scientifique, and partially funded by this organization via the Institut National des Sciences de l'Univers. The University of Minnesota contribution to this experiment is funded by NASA contract 5-29313.

We wish to thank the many dedicated people who have, over the years, contributed to the success of the Ulysses mission. Without the tireless help of administrative and support staff in the collaborating laboratories, the experiment would never have been realized. The URAP team wishes to acknowledge in particular the contributions of past and present members of the ESA and NASA Ulysses team, who first had to overcome the frustrations and limitations caused by a descoping of the original mission, and then endured the long delays introduced by circumstances beyond their control.

> "The ultimate measure of a man is not where he stands in moments of comfort and convenience, but where he stands in moments of challenge and controversy".
>
> -Martin Luther King, Jr

## References

Birmingham T.J., Alexander J.K., Desch M.D., Hubbard R.F., Pedersen B.M. 1981, J. Geophys. Res. 86, 8497

Bhonsle R.V., Alurkar S.K., Degaonkar S.S., Vats H.O., Sharma A.K. 1986, Exploration of the heliosphere by interplanetary scintillation, in The Sun and the Heliosphere in Three Dimensions, Marsden R.G. Ed., Proc. XIXth ESLAB Symposium, (D. Reidel) 153

Bougeret J.-L., Fainberg J., Stone R.G. 1983, Science 222, 506

Burlaga L.F., McDonald F.B., Ness N.F., Lazarus A.J. 1991, J. Geophys. Res., in press

Carr *et al.* 1983, Physics of the Jovian Magnetosphere, A.J. Dessler Ed. (Cambridge University Press, New York) 226

Chateau Y., Meyer-Vernet N. 1991, J. Geophys. Res., 96, 5825.

Coles W.A., Rickett B.J. 1986, Interplanetary scintillation observations of the solar wind at high latitudes, in The Sun and the Heliosphere in Three Dimensions, Marsden R.G. Ed., Proc. XIXth ESLAB Symposium (D. Reidel) 143

Couturier P., Hoang S., Meyer-Vernet N., Steinberg J.-L. 1981, J. Geophys. Res. 86, 127

Dulk G.A. 1985, ARA&A 23, 169

Dulk G.A., Steinberg J.-L., Hoang S., Goldman M.V. 1987, A&A 173, 366

Etcheto J., Faucheux M. 1984, J. Geophys. Res. 89, 6631

Fainberg J., Evans L.G., Stone R.G. 1972, Science 178, 743

Fainberg J., Hoang S., Manning R. 1985, A&A 153, 145

Fainberg J., Stone R.G. 1970, Solar Phys. 15, 433

Fitzenreiter R.J., Fainberg J., Weber R.R., Alverez H., Haddock F.T., Potter W.H. 1977, Solar Phys. 52, 465

Fry C.D., Akasofu S. 1986, Three-dimensional structure of the heliospheric current sheet, in The Sun and the Heliosphere in Three Dimensions, Marsden R.G. Ed., Proc. XIXth ESLAB Symposium (D. Reidel) 153

Gurnett D.A., Goertz C.K. 1983, Geophys. Res. Let. 10, 587

Gurnett D.A., Anderson R.R., Scarf F.L., Kurth W.S. 1978, J. Geophys. Res. 83, 4147

Gurnett D.A., Frank L.A. 1978, J. Geophys. Res. 83, 58

Gurnett D.A., Maggs J.E., Gallagher D.L., Kurth W.S., Scarf F.L. 1981, J. Geophys. Res. 86, 8833

Harvey C.C., Etcheto J., Mangeney A. 1979, Space Sci. Rev. 23, 39

Hoeksema J.T. 1986, Exploration of the heliosphere by interplanetary scintillation, Proc. The Sun and the Heliosphere in Three Dimensions, XIXth ESLAB Symposium, Les Diablerets, Switzerland, Marsden R.G. Ed. (D. Reidel Publishing Co.) 241

Jokipii J.R., Kota, J. Geophys. Res. Lett. 16, 1

Jones D. & Leblanc Y. 1986, Ann. Geophys., 87, A29

Kurth W.S. 1980, Geophys. Res. Let. 7, 57

Lengyel-Frey D. & Stone R.G. 1989, J. Geophys. Res. 94, 159

Lin R.P. 1985, Solar Phys. 100, 537

Lin R.P., Potter D.W., Gurnett D.A., Scarf F.L. 1981, ApJ 257, 364

MacDowall R.J. 1989, Geophys. Res. Let. 16, 923

Manning R., Fainberg J. 1980, Space Sci. Instr. 5, 161

Meyer-Vernet N., Perche C. 1989, J. Geophys. Res. 94, 2405

Meyer-Vernet N., Couturier P., Hoang S., Steinberg J.-L. 1986, J. Geophys. Res. 91, 3294

Parker E.N. 1963, Interplanetary Dynamical Processes, Interscience Publishers

Scarf F.L., Gurnett D.A., Kurth W.S. 1979, Science 204, 991

Sittler E.C., Strobel D.F. 1987, J. Geophys. Res. 92, 5741

Thorne R.M., Moses J. 1983, Geophys. Res. Let. 10, 631

Trotignon J.G., Echeto J., Thouvenin J.P. 1986, J. Geophys. Res. 91, 4302

Wang Y.-M., Sheeley N.R. Jr., Nash A.G. 1990, Nature 347, 439

Warwick J.W., Pearce J.B., Riddle A.C., Alexander J.K., Desch M.D., Kaiser M.L., Thieman J.A., Carr T.D., Gulkis S., Boischot A., Leblanc Y., Pedersen B.M., Staelin D.H. 1979, Science 206, 991 and 204, 955

Zarka P. 1991, The Auroral Radio Emissions from Planetary Magnetospheres, COSPAR, Adv. Space Res., in press

TABLE 1. *Characteristics of the unified radio and plasma wave experiment.*

| Instruments and Bands | Measurements | Frequency Range | Maximum Channels | Channel Bandwidth | Data or Spectrum Time Resolution | Dynamic Range | Sensitivity (rms) |
|---|---|---|---|---|---|---|---|
| Radio Astronomy Receiver (RAR) Hi | $E_z$ and $E_x+E_z$($\delta=0$) plus $E_x+E_z$($\delta=90$) at 1024 bps<br>- OR -<br>$E_x$ and $E_z$ only | 52-940 kHz | 12 | 3 kHz | 8 samples/spin for 3 frequencies at 1024 bps | 70 dB (power) + 20 dB Jupiter attenuator | 10 nV/Hz$^{1/2}$ @ 100 kHz |
| Lo |  | 1.25-48.5 kHz | 64 | 750 Hz | 12 samples/spin for 1 frequency at 1024 bps |  | 30 nV/Hz$^{1/2}$ @ 10 kHz |
| Plasma Frequency Receiver (PFR) | Peak $E_x$, Ave. $E_x$ & Ave. $E_z$ | 0.57-35 kHz | 32 log-spaced by 14% | 14% of center frequency | 16 frames* used to transmit 1 set of spectra | 2 μ V to 3 Volts per channel | 100 nV/Hz$^{1/2}$ @ 10 kHz |
| Waveform Analyzer (WFA) (FFT-DPU) Hi | Ave., Peak & relative phase of $E_x$, $B_Y$ & ($E_z$ or $B_z$) | 8-448 Hz | 12 log-spaced by 25% | 25% of center frequency | 1 set of spectra/ 2 formats* for 4 directions or sectors | 90 dB (power) | E: 2μ V/Hz$^{1/2}$ @ 100 Hz<br>B: 0.03pT/ Hz$^{1/2}$ @ 100 Hz |
| Lo | Ave. & relative phase of $E_x$ & ($B_Y$ or $B_z$) | 0.08-5.3 Hz | 12 log-spaced by 25% | 25% of center frequency | 1 set of spectra/ 16 frames* | 90 dB (power) |  |
| Fast Envelope Sampler (FES) Hi | $E_x$ or $E_z$ | 0.6-60 kHz | 1of 3 | E: Extends from $f_{min}$ to 10 times $f_{min}$ | 1 sample/1.2 ms (fastest rate) 1024 samples/ event | 64 dB plus 32 dB attenuator | $E_x$: 250μ V<br>$E_z$: 60μ V<br>B: 2pT |
| Lo | $E_x$, $E_z$ or ($B_Y$ or $B_z$) | E: 0.1-20 kHz<br>B: 10-600 Hz | 1of 4<br>1of 1 |  |  |  |  |
| "DC" | Outputs of X and Z PFR preamps for monitoring DC potential & low freq. fluctuations. Fixed angle & scan measurements. |  |  |  |  |  |  |
| Sounder | 30 Volt pulse applied to X antenna for 1.33 ms. Low frequency RAR steps through 64 frequencies in 128 sec. Twelve point spectrum for each frequency step yields 768 linearly spaced frequencies between 1.25 & 48.5 kHz. |  |  |  |  |  |  |
| Antennas | $E_X$: two 35 m monopoles, 72.5 m tip-to-tip, 5x0.04 mm cross section; $E_z$: 7.5 m monopole, 25 mm cross-section; B: 2-axis search coils. |  |  |  |  |  |  |
| Notes | *At 1024 bps, 1 frame of data=1 sec.; 32 frames = 1 format.<br>RAR: Can measure full polarization (4 Stokes parameters) plus source direction & angular size. Commandable frequency lists, including linear sweep (Lo band) & freeze modes. Spin period ~12 sec.<br>WFA: Average spectra for each octant in Hi band are grouped with opposing octant.<br>FES: Largest 1024 point event telemetered each 49 formats.<br>Sounder: Uses FFT-DPU when active; displaces WFA and some PFR telemetry. |  |  |  |  |  |  |

TABLE 2. *Typical noise figures for the radio receiver preamplifiers.*

| Sensitivity (μV) | Frequency (kHz) | Bandwidth (kHz) |
|---|---|---|
| 2.20 | 1 | 0.75 |
| 0.15 | 30 | 0.75 |
| 0.20 | 150 | 3.00 |
| 0.30 | 940 | 3.00 |

TABLE 3. *Combined search coil and preamp sensitivity, bandwidth, and gain.*

| Sensitivity (pT rms/√Hz) | Frequency (Hz) |
|---|---|
| $200\times10^{-2}$ | 1 |
| $20\times10^{-2}$ | 10 |
| $3\times10^{-2}$ | 100 |
| $1\times10^{-2}$ | 500 |
| **Bandwidth** | **Gain:** |
| 10Hz to 500 Hz at -3dB;<br>-6dB per octave from 10 Hz to 1Hz | 0.3V/nT from 10 Hz - 500 Hz |

TABLE 4. *Possible RAR high band frequencies (kHz).*

|  |  |  |  |  |  |  |  |  |  |  |  |
|---|---|---|---|---|---|---|---|---|---|---|---|
| 52 | 63 | 81 | 100 | 120 | 148 | 196 | 272 | 387 | 540 | 740 | 940 |

TABLE 5. *PFR frequencies in kHz.*

| Cnannel # | Frequency | Channel # | Frequency |
|---|---|---|---|
| 1 | 0.570 | 17 | 4.773 |
| 2 | 0.651 | 18 | 5.451 |
| 3 | 0.743 | 19 | 6.226 |
| 4 | 0.849 | 20 | 7.110 |
| 5 | 0.970 | 21 | 8.120 |
| 6 | 1.107 | 22 | 9.273 |
| 7 | 1.265 | 23 | 10.590 |
| 8 | 1.444 | 24 | 12.095 |
| 9 | 1.649 | 25 | 13.813 |
| 10 | 1.884 | 26 | 15.775 |
| 11 | 2.151 | 27 | 18.016 |
| 12 | 2.457 | 28 | 20.575 |
| 13 | 2.806 | 29 | 23.498 |
| 14 | 3.205 | 30 | 26.835 |
| 15 | 3.660 | 31 | 30.647 |
| 16 | 4.180 | 32 | 35.000 |

TABLE 6. *The 12 log-spaced band centers of the WFA (>10 Hz band) in Hz.*

| | | | | | | | | | | | |
|---|---|---|---|---|---|---|---|---|---|---|---|
| 9 | 14 | 19 | 28 | 37 | 56 | 75 | 112 | 149 | 224 | 299 | 448 |

TABLE 7. *Center frequencies for the WFA (< 10 Hz band) in Hz.*

| | | | | | | | | | | | |
|---|---|---|---|---|---|---|---|---|---|---|---|
| 0.08 | 0.16 | 0.22 | 0.33 | 0.44 | 0.66 | 0.88 | 1.33 | 1.77 | 2.66 | 3.55 | 5.33 |

TABLE 8. *The Fast Envelope Sampler commandable frequency bands.*

| | | | | |
|---|---|---|---|---|
| High Bands | 600Hz -6 kHz | 2 kHz- 20 kHz | 6 kHz- 60 kHz | |
| Low Bands | 10 Hz-1kHz | 200 Hz-2kHz | 600 Hz-6 kHz | 2 kHz-20 kHz |

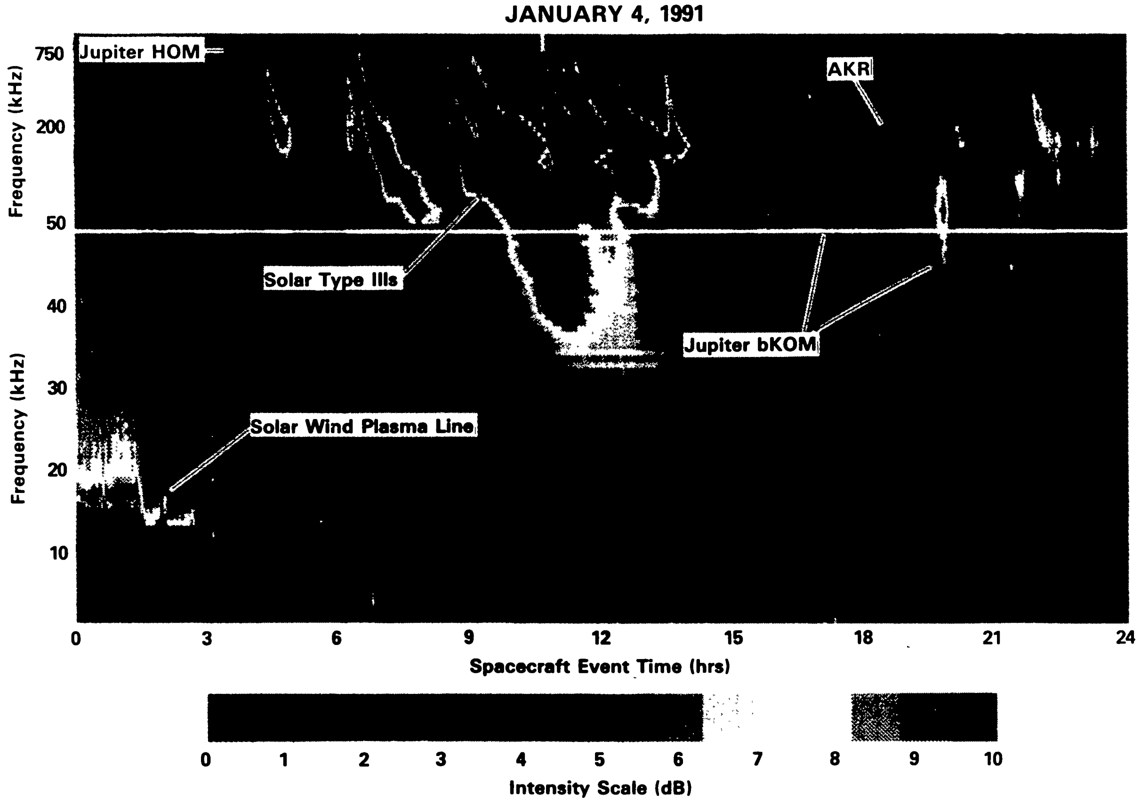

FIGURE 1. Dynamic spectrum observed on January 4, 1991 with the Radio Astronomy Receiver. The abscissa is the spacecraft event time and the ordinate scale shows observing frequency. An intensity scale is included in the figure. A horizontal white line divides the observations of the high frequency (upper part of the figure) and low frequency (lower part of the figure) sections of this receiver. Note that the high frequency data are on a log frequency scale while the low frequency data are on a linear frequency scale. The figure demonstrates the wide variety of phenomena which are observed with this one instrument. Examples of type III solar radio bursts, auroral kilometric radiation, Jupiter emissions and the thermal plasma line can be seen in the figure. In Section 3, each of these phenomena will be discussed in greater detail along with observations from the other URAP instruments.

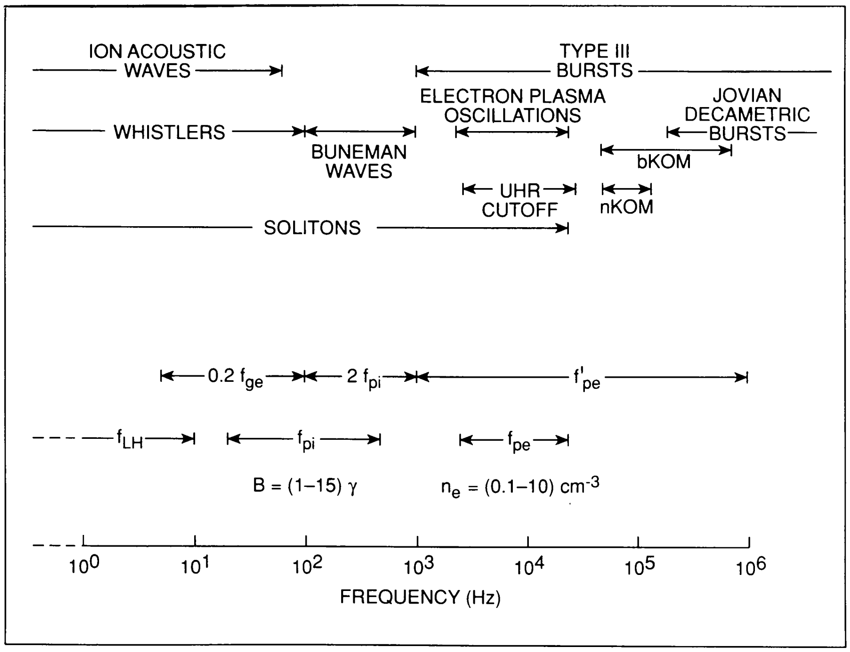

FIGURE 2. Characteristic wave modes and frequencies anticipated during the Ulysses mission, based on expected magnetic field strength and particle density ranges. The locally measured electron plasma frequency $f_{pe}$ is distinguished from the remotely measured $f'_{pe}$. The terms $f_{ge}$, $f_{pi}$, $f_{LH}$ and $f_{UHR}$ refer to the electron gyro, ion plasma, lower hybrid and upper hybrid resonance frequencies, respectively. Typical ranges are also shown for type III solar radio bursts and Jovian bKOM, nKOM, and decametric bursts.

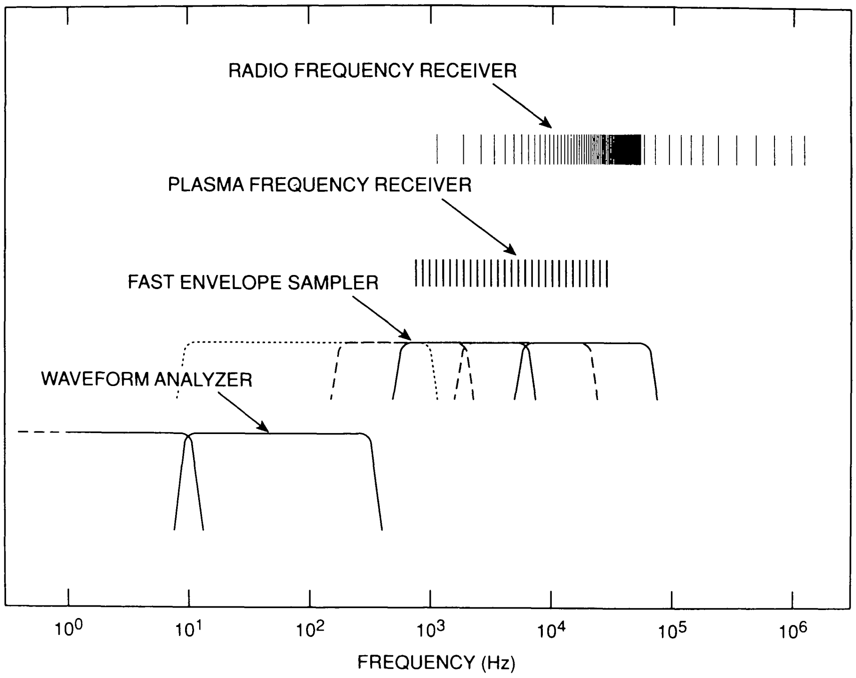

FIGURE 3. Frequency coverage of the Ulysses Radio Astronomy Receivers (RAR), Plasma Frequency Receiver (PFR), Fast Envelope Sampler (FES) and Waveform Analyzer (WFA) are shown.

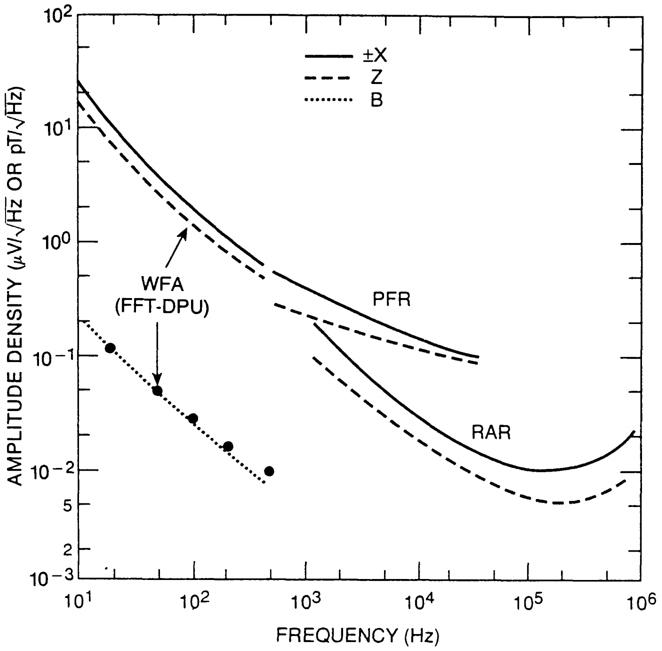

FIGURE 4. Sensitivity of the URAP experiment. The electric antenna figures are referred to the receiver input ports since the transfer "gain" is a function of the ambient plasma parameters. The $\pm X$ signal levels are higher than the $Z$ levels because two preamplifiers are involved instead of one. The 10-500 Hz range is measured by the Waveform Analyzer (FFT-DPU), the 0.57-35 kHz range by the Plasma Frequency Receiver (PFR) and the 1.25-940 kHz range by the Radio Receiver (RAR). The closed circles on the magnetic antenna curve are in-flight calibration values.

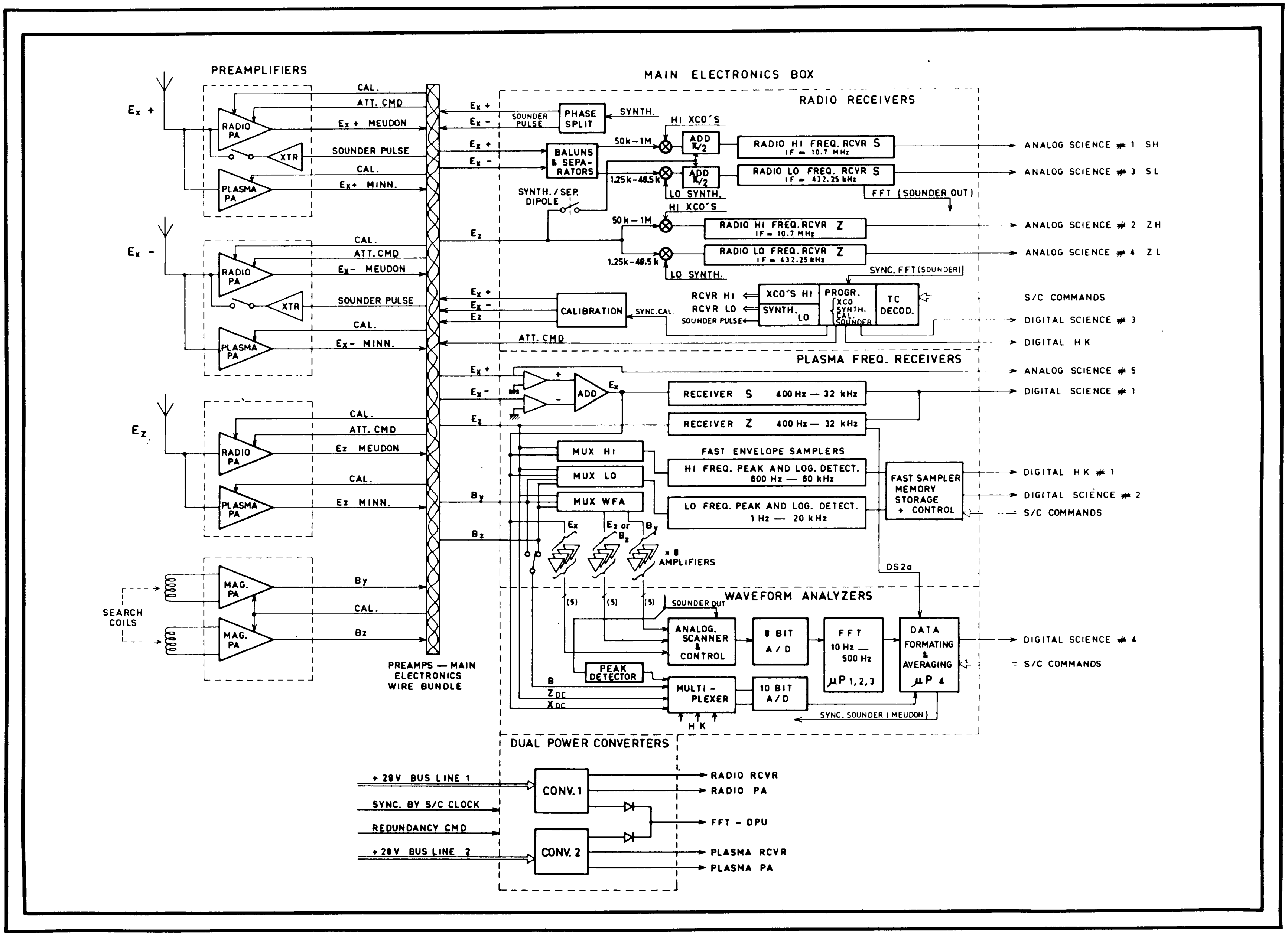

FIGURE 5. Block diagram of the Unified Radio and Plasma Wave instrument on Ulysses. The diagram shows the various electric and magnetic antennas and preamplifiers and how the antennas are connected to the RAR, PFR, FES, WFA and Sounder. The power converters and calibration systems, as well as the phase shift networks required for direction & polarization measurements, are also shown.

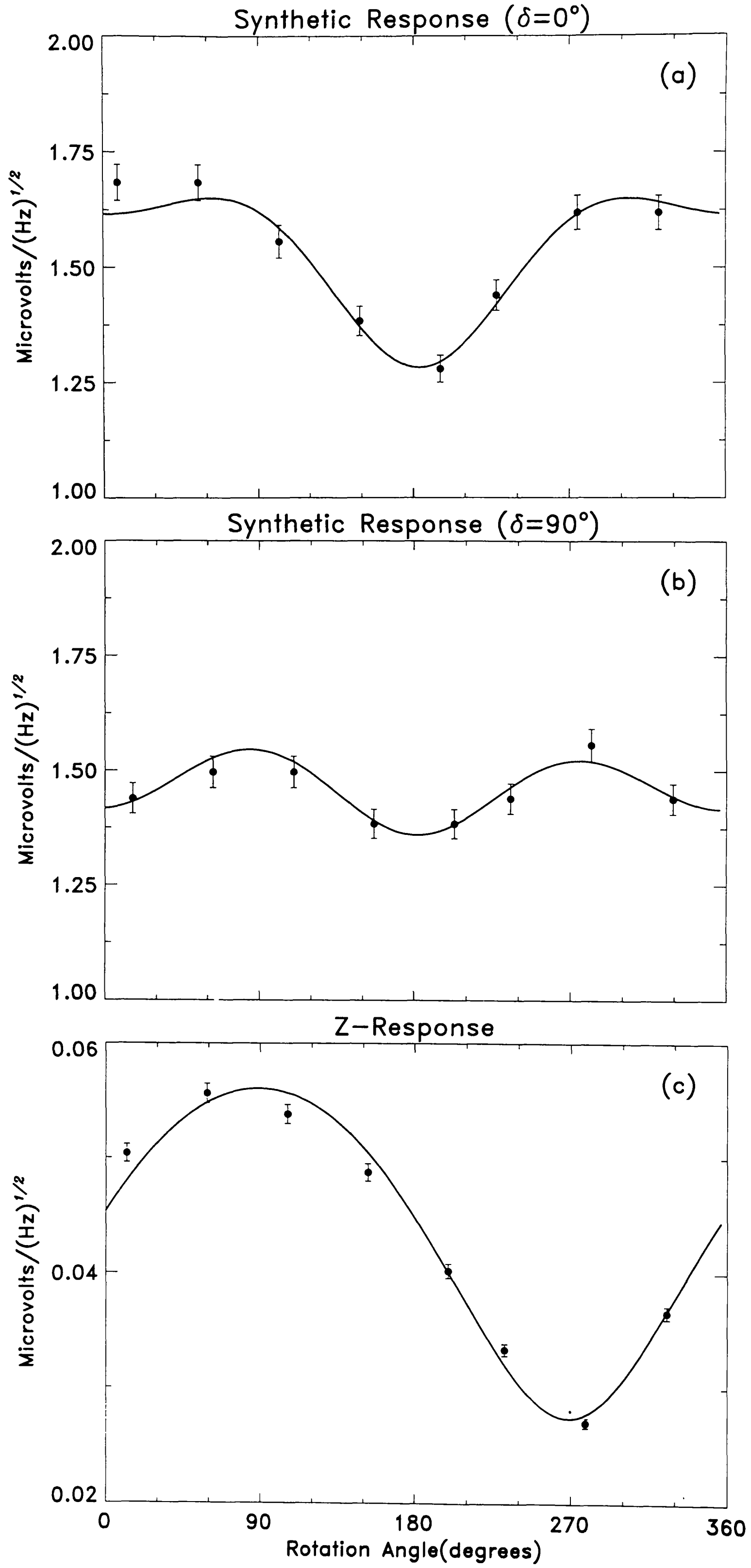

FIGURE 6. A simultaneous fit to analytic equations for the three antenna responses, over one s/c rotation, are required to determine source direction, angular size, and polarization state. The analysis for this event, which occured on December 9, 1990 at 06:20 UT, yields a radio source with an angular radius of 25° and a radio centroid located 4° to the west of the spacecraft-Sun line and about 0.5° above the ecliptic plane.

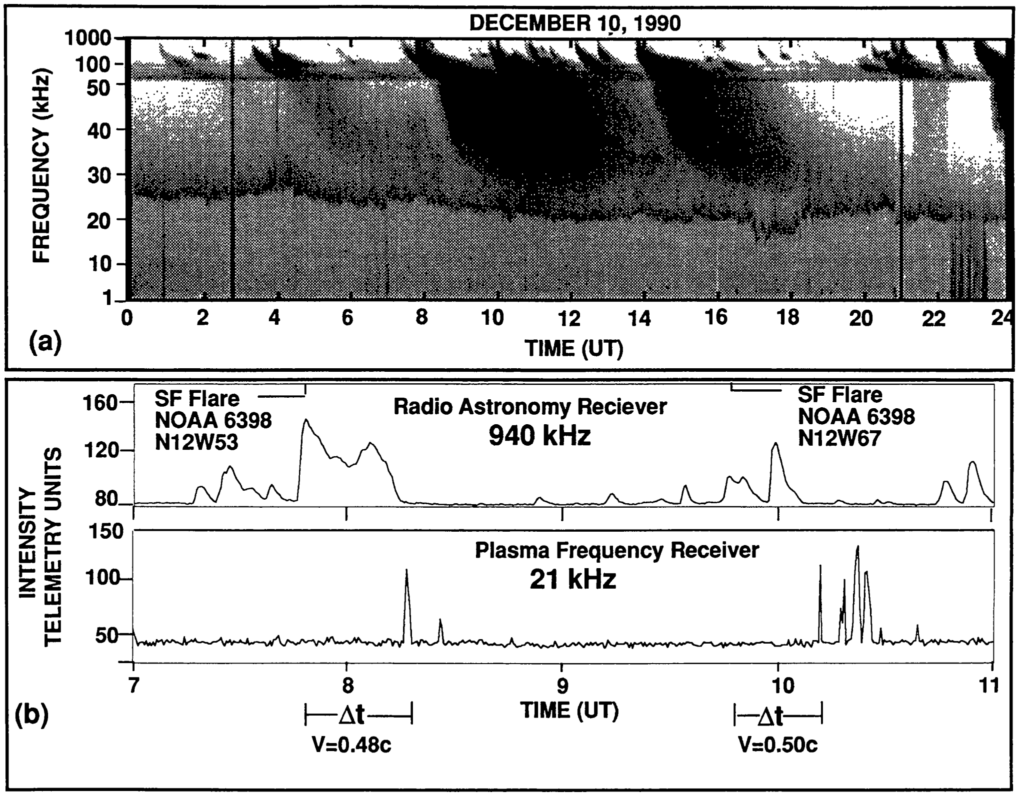

FIGURE 7. Dynamic spectrum, obtained with the RAR and $E_x$ antenna (panel a) on December 10, 1990. Panel b shows intensity *versus* time profiles from 7:00 UT to 11:00 UT obtained at 940 kHz with the RAR (top of panel) and at 21 kHz with the PFR. Note the bursts of Langmuir waves starting at about 8:17 UT and at 10:13 UT due to the passage at the spacecraft of the exciter electron stream.

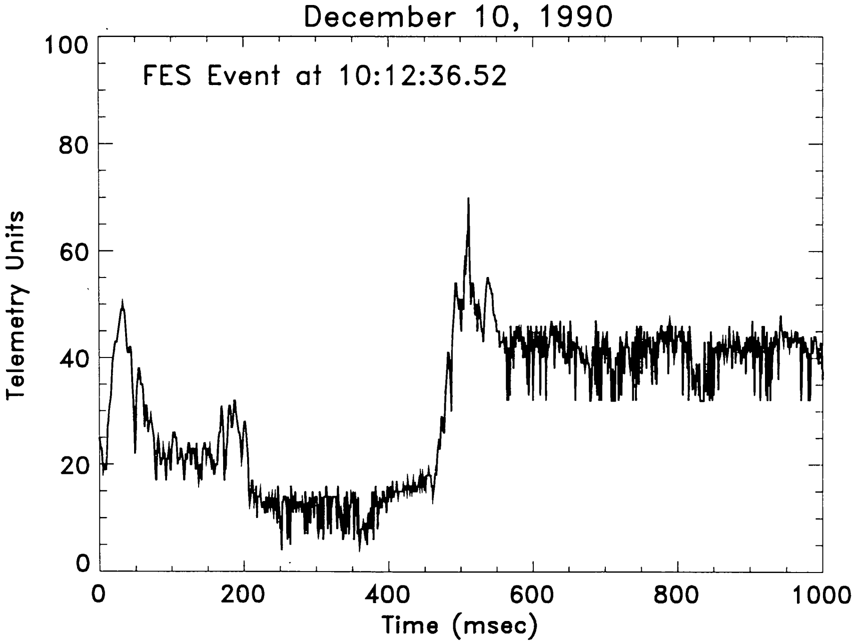

FIGURE 8. The Langmuir waves observed in Figure 7b can be studied in greater detail with the FES. An event detected in the 6-60 kHz range at 10:12:36.5 UT, is shown in this figure. Each sample along the abscissa is 1.12 msec so that the entire sweep of the 1024 data points corresponds to 1.15 seconds. After the large event at the center of the figure at about 500 msec., a 32 dB attenuator was switched in. This also increases the noise level, so that all of the data after about 550 msec are receiver noise. The peak signal is 7 mV/m.

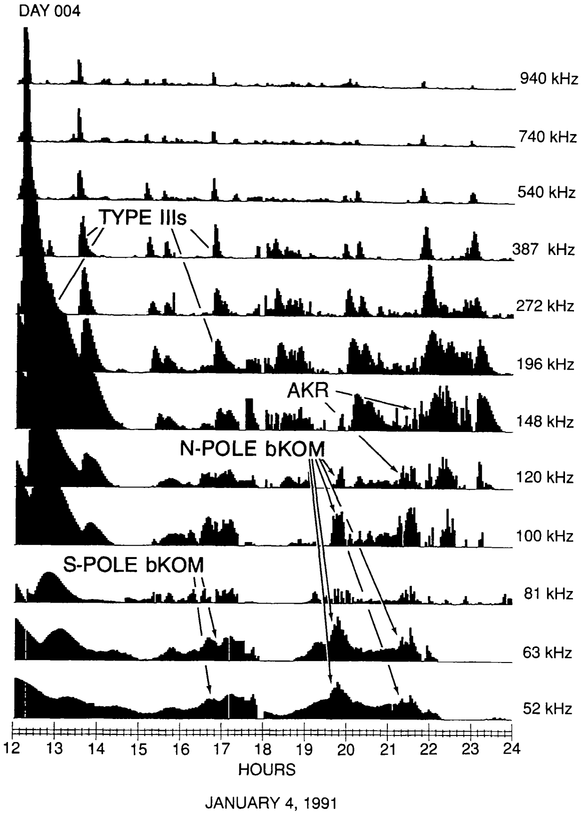

FIGURE 9. Intensity *versus* time plots for observing frequencies from 52 kHz to 940 kHz for January 4, 1991. In addition to the occurrence of frequent solar radio bursts, terrestrial auroral kilometric radiation is observed at 196 kHz from approximately 20:00 to 24:00 UT. Jovian broad band kilometric radiation (bKOM) is apparently observed from *both poles* at frequencies from 52 kHz to 120 kHz. The South pole bKOM occurs at approximately 45° CML and the North pole bKOM at approximately 200° CML.

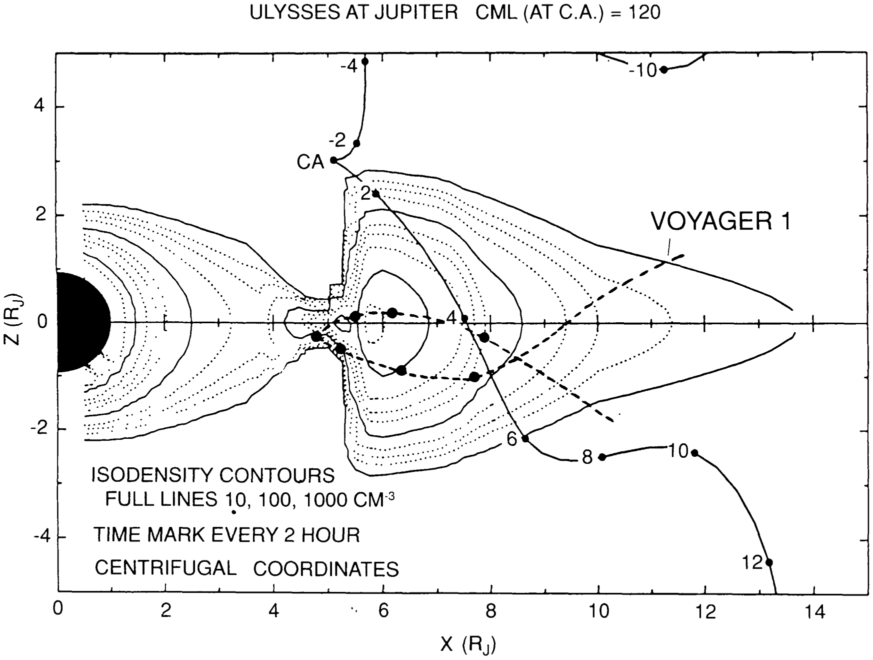

FIGURE 10. This figure shows the trajectory of Ulysses past Jupiter and through the Io torus. For comparison the Voyager 1 trajectory is also shown. The URAP experiment will be able to determine the source locations, angular sizes and polarizations of the various Jupiter radio sources as well as the properties of the Io torus along the spacecraft trajectory. (CML is Central Meridian Longitude.)

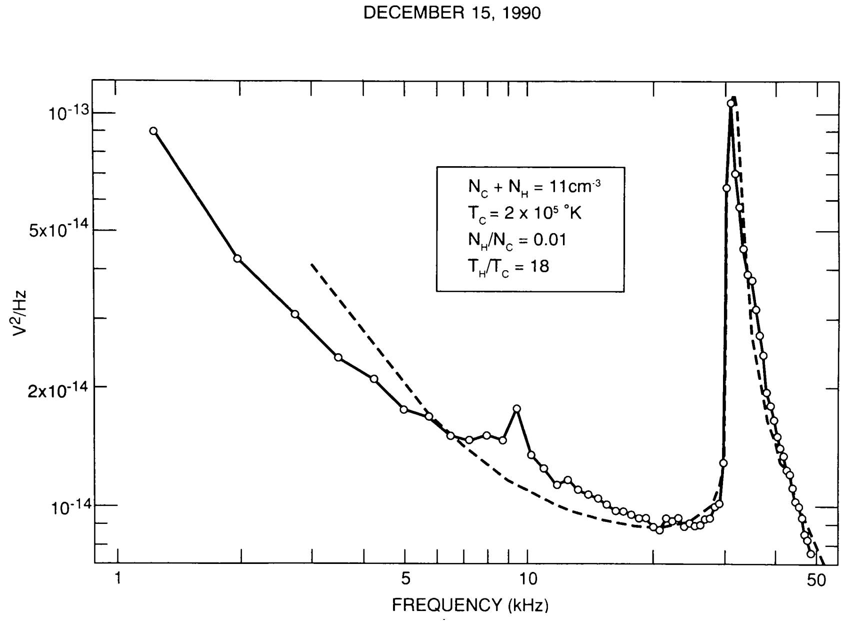

FIGURE 11. Quasi-thermal noise spectrum obtained with the long $X$ antenna and the low-frequency receiver on 15 December 1990 at 01:02 UT. The dotted line represents a preliminary calculation of the theoretical spectrum, assuming a bi-Maxwellian electron distribution with parameters: total density $n_c + n_h = 11/\text{cm}^3$, cold electron temperature $T_c = 2 \times 10^5$ K, "hot" to "cold" electron density ratio, $n_h/n_c = 0.01$, with the temperature ratio $T_h/T_c = 18$, which is the best preliminary fitting. The peak at the plasma frequency is the plasma thermal noise; the low-frequency rising part results from shot noise due to absorption and emission of electrons on the antenna surface.

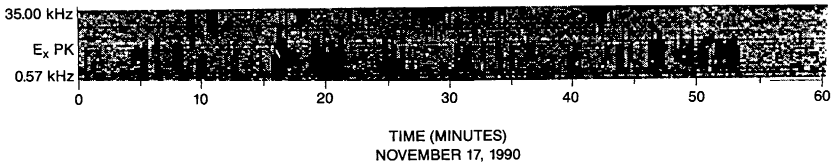

FIGURE 12. Dynamic spectrum of approximately one hour of data on November 17, 1990, from the PFR showing intense Langmuir waves at the high frequencies and ion acoustic-like noise at the low frequencies in the figure. The apparent anticorrelation between the occurence of the Langmuir waves and the ion acoustic-like noise appears to be unusual.

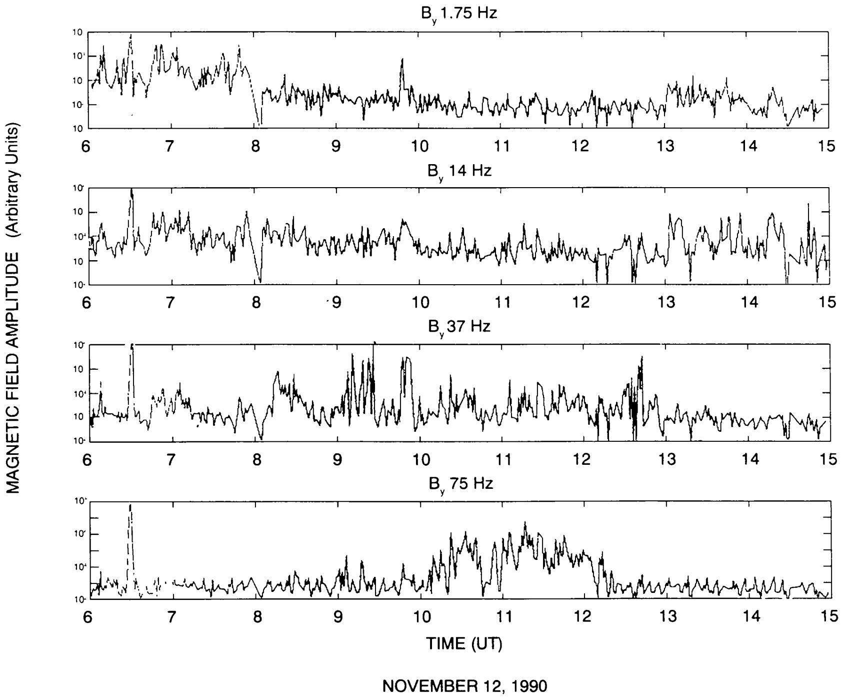

FIGURE 13. Evolution of the amplitude of the magnetic component $B_y$ (from the WFA) at 4 different frequencies for the event of November 12, 1990. A density discontinuity occurred at about 06:50 UT followed by numerous density variations.

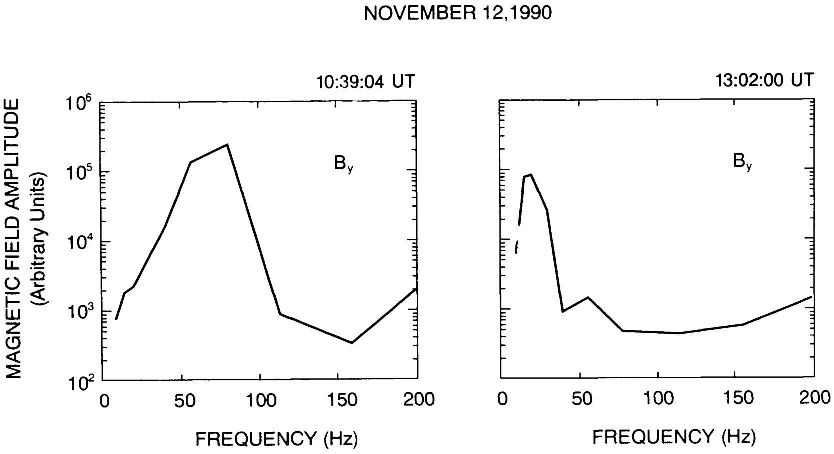

FIGURE 14. Detailed spectra averaged over 64 seconds of data taken at two different times, 10:39:04 and 13:02:00 UT, for the event shown in Figure 14.

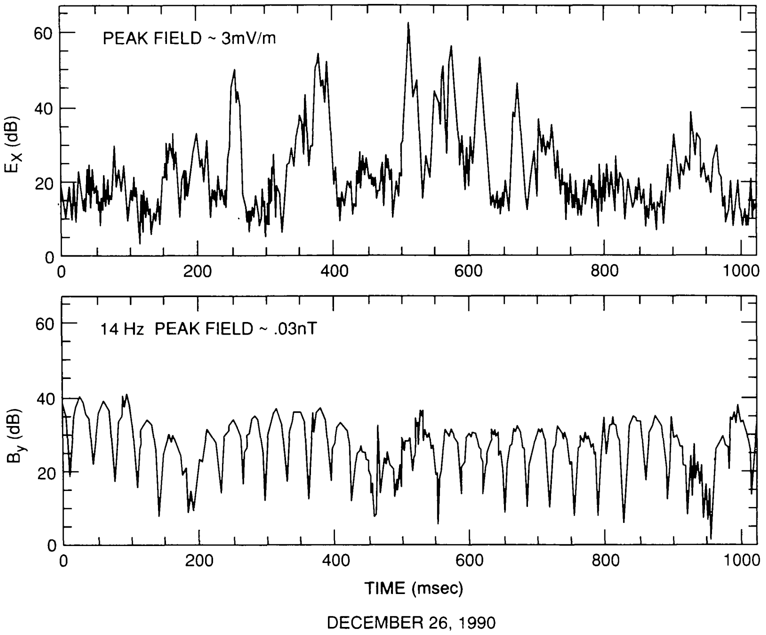

FIGURE 15. An FES event showing presumably whistler mode in the magnetic search coil at 14 Hz (lower panel) with electric fields (upper panel) observed on December 26, 1990. The scale values are in dB. The peak electric field strength is about 3 mV/m and the magnetic field is about 0.03 nT.

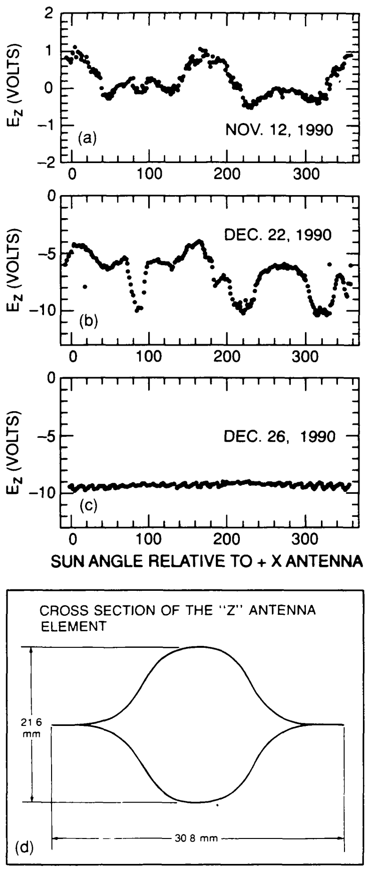

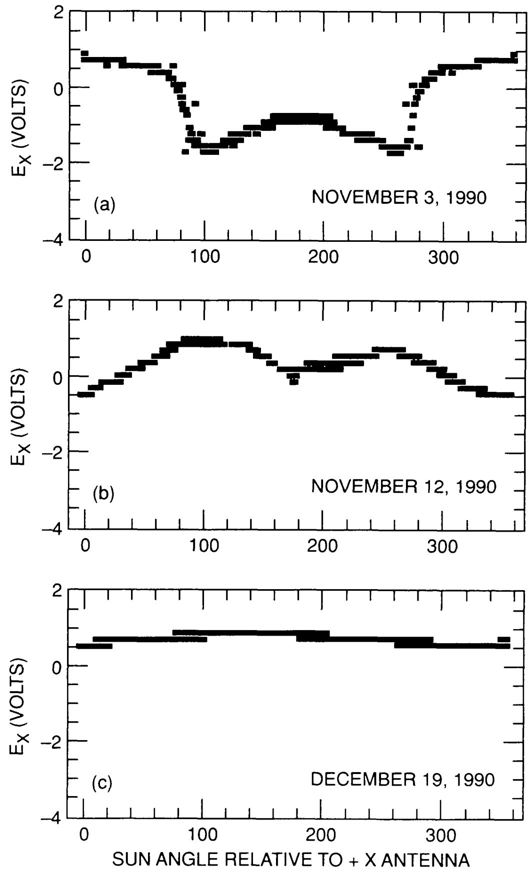

FIGURE 16. Variation of potential on the $Z$ antenna as a function of Sun angle. Panel a) shows the complex signal generated by photoemission when the antenna was inclined about 45° to the Sun on November 12, 1990. Panel b) for December 22, 1990 shows the beginning of more complete shadowing by the Sun, while panel c) shows complete shadowing by December 26, 1990. Part of the variations seen is due to the non-uniform $Z$ antenna cross section as illustrated in panel d).

FIGURE 17. Potential on the $+X$ electric monopole as a function of rotation angle at various times. Panel a), for November 3, 1990, shows the potential *before* deployment of the $X$ antenna. Panels b) (November 12, 1990) and c) (December 19, 1990) show reduction of the photoelectric variations as Ulysses turns to face the Sun.

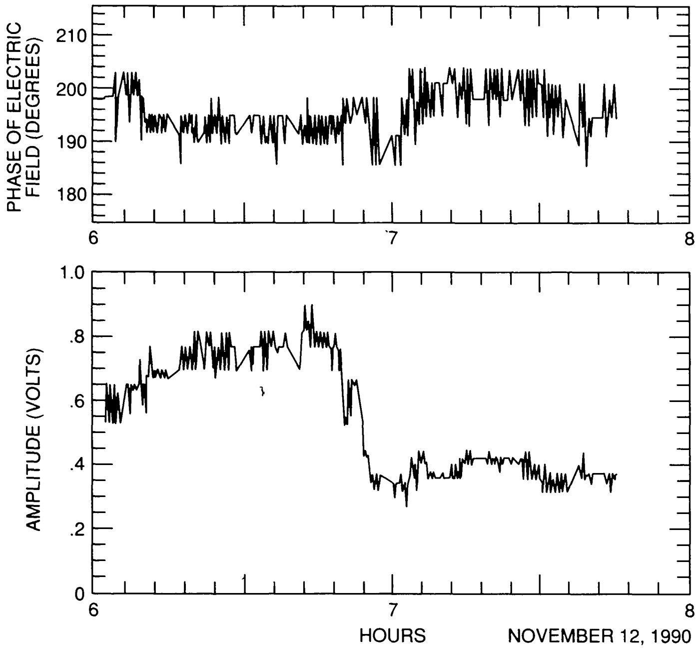

FIGURE 18. Potential difference on the $E_X$ dipole on November 12, 1990. The upper panel shows phase angle and the lower panel amplitude. There was a rapid increase of plasma density by a factor of about 4, at approximately 07:00 UT.

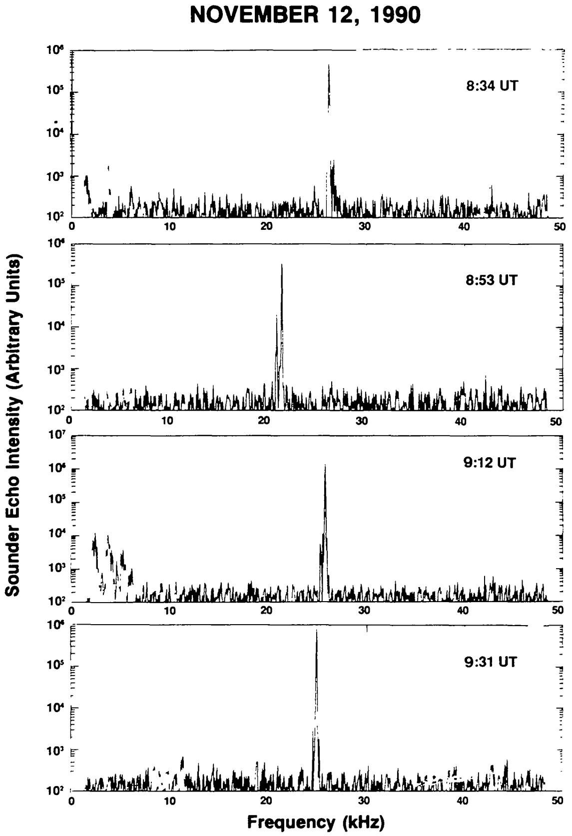

FIGURE 19. Sounder echo at four separated times showing shift in resonant frequency as the local plasma density changes. The sharpness of the echo illustrates the ability of a sounder to accurately determine the local density. The natural noise observed in the 3-5 kHz range at 9:12 UT also illustrates the high spectral resolution possible with this system.